PUBLICATIONS OF THE ASTRONOMICAL SOCIETY OF THE PACIFIC, **121**:559–576, 2009 June
© 2009. The Astronomical Society of the Pacific. All rights reserved. Printed in U.S.A.

GOALS: The Great Observatories All-Sky LIRG Survey

L. ARMUS,[1] J. M. MAZZARELLA,[2] A. S. EVANS,[3,4] J. A. SURACE,[1] D. B. SANDERS,[5] K. IWASAWA,[6] D. T. FRAYER,[7] J. H. HOWELL,[1] B. CHAN,[2] A. PETRIC,[1] T. VAVILKIN,[8] D. C. KIM,[3] S. HAAN,[1] H. INAMI,[9] E. J. MURPHY,[1] P. N. APPLETON,[7] J. E. BARNES,[5] G. BOTHUN,[10] C. R. BRIDGE,[1] V. CHARMANDARIS,[11] J. B. JENSEN,[12] L. J. KEWLEY,[5] S. LORD,[2] B. F. MADORE,[2,13] J. A. MARSHALL,[14] J. E. MELBOURNE,[15] J. RICH,[5] S. SATYAPAL,[16] B. SCHULZ,[7] H. W. W. SPOON,[17] E. STURM,[18] V. U,[5] S. VEILLEUX,[19] AND K. XU[7]

Received 2009 March 4; accepted 2009 April 27; published 2009 June 4

ABSTRACT. The Great Observatories All-Sky LIRG Survey (GOALS[20]) combines data from NASA's *Spitzer Space Telescope, Chandra X-Ray Observatory, Hubble Space Telescope* (*HST*), and *Galaxy Evolution Explorer* (*GALEX*) observatories, together with ground-based data, into a comprehensive imaging and spectroscopic survey of over 200 low-redshift ($z < 0.088$), Luminous Infrared Galaxies (LIRGs). The LIRGs are a complete subset of the *IRAS* Revised Bright Galaxy Sample (RBGS), which comprises 629 extragalactic objects with 60 μm flux densities above 5.24 Jy, and Galactic latitudes above five degrees. The LIRGs targeted in GOALS span the full range of nuclear spectral types defined via traditional optical line-ratio diagrams (type-1 and type-2 AGN, LINERs, and starbursts) as well as interaction stages (major mergers, minor mergers, and isolated galaxies). They provide an unbiased picture of the processes responsible for enhanced infrared emission in galaxies in the local Universe. As an example of the analytic power of the multiwavelength GOALS data set, we present *Spitzer, Chandra, HST,* and *GALEX* images and spectra for the interacting system VV 340 (*IRAS* F14547 + 2449). The *Spitzer* MIPS imaging data indicates that between 80–95% of the total far-infrared emission (or about 5×10^{11} $L_{\odot}$) originates in VV 340 north. While the *Spitzer* IRAC colors of VV 340 north and south are consistent with star-forming galaxies, both the *Spitzer* IRS and *Chandra* ACIS data indicate the presence of an AGN in VV 340 north. The observed line fluxes, without correction for extinction, imply that the AGN accounts for less than 10%–20% of the observed infrared emission. The X-ray data are consistent with a heavily absorbed ($N_H \geq 10^{24}$ cm^{-2}) AGN. The GALEX far and near-UV fluxes imply a extremely large infrared "excess" (IRX) for the system ($F_{IR}/F_{fuv} \sim 81$) which is well above the correlation seen in starburst galaxies. Most of this excess is driven by VV 340 N, which has an IR excess of nearly 400. The VV 340 system seems to be comprised of two very different galaxies: an infrared luminous edge-on galaxy (VV 340 north) that dominates the long-wavelength emission from the system, which hosts a buried AGN; and a face-on starburst (VV 340 south) that dominates the short-wavelength emission.

1. INTRODUCTION

The *Infrared Astronomical Satellite* (*IRAS*) provided the first unbiased survey of the sky at mid and far-infrared wavelengths, giving us a comprehensive census of the infrared emission properties of galaxies in the local Universe. The high luminosity tail of the infrared luminosity function can be approximated by a power law ($L_{IR}^{-2.35}$), which implies a space density for the most

[1] Spitzer Science Center, California Institute of Technology, Pasadena, CA 91125
[2] Infrared Processing and Analysis Center, California Institute of Technology, Pasadena, CA 91125
[3] National Radio Astronomy Observatory, Charlottesville, VA 22903
[4] Department of Astronomy, University of Virginia, Charlottesville, VA 22904
[5] Institute for Astronomy, University of Hawaii, Honolulu, HI 96822
[6] INAF-Observatorio Astronomico di Bologna, Via Ranzani 1, Bologna, Italy
[7] NASA Herschel Science Center, California Institute of Technology, Pasadena, CA 91125
[8] Department of Physics and Astronomy, SUNY Stony Brook, Stony Brook, NY 11794
[9] Department of Space and Astronautical Science, The Graduate University for Advanced Studies, Japan
[10] Physics Department, University of Oregon, Eugene, OR 97402
[11] Department of Physics, University of Crete, P.O. Box 2208, GR-71003, Heraklion, Greece
[12] Gemini Observatory, Tucson, AZ, 85719
[13] The Observatories, Carnegie Institute of Washington, Pasadena, CA 91101
[14] The Jet Propulsion Laboratory, California Institute of Technology, Pasadena, CA 91125
[15] California Institute of Technology, Pasadena, CA 91125
[16] Department of Physics & Astronomy, George Mason University, Fairfax, VA 22030
[17] Department of Astronomy, Cornell University, Ithaca, NY 14953
[18] MPE, Postfach 1312, 85741 Garching, Germany
[19] Astronomy Department, University of Maryland, College Park, MD 20742
[20] See http://goals.ipac.caltech.edu.

luminous infrared sources that is well in excess of what is found in the optical for local galaxies (e.g., Schechter 1976). At the highest luminosities, Ultraluminous Infrared Galaxies, or ULIRGs (those galaxies with $L_{\rm IR} > 10^{12}\ L_{\odot}$) have a space density that is a factor of 1.5–2 higher than that of optically selected QSOs, the only other known objects with comparable bolometric luminosities (Schmidt & Green 1983).

Multiwavelength imaging surveys have shown that nearly all ULIRGs are found in systems that have undergone strong tidal perturbations due to the merger of pairs of gas-rich disk galaxies (Armus et al. 1987; Sanders et al. 1988a, 1988b; Murphy et al. 1996, 2001a). They have enhanced star formation rates compared to noninteracting galaxies, and the fraction of sources with active galactic nuclei (AGN) increases as a function of increasing $L_{\rm IR}$ (Armus et al. 1989; Murphy et al. 1999, 2001b; Veilleux et al. 1995, 1997; Kim et al. 1998). ULIRGs may represent an important evolutionary stage in the formation of QSOs (e.g., Sanders et al. 1988a, 1988b) and perhaps powerful radio galaxies (Mazzarella et al. 1993; Evans et al. 2005). In fact, numerical simulations have shown that tidal dissipation in mergers can be very effective in driving material from a gas-rich galaxy disk toward the nucleus, fueling a starburst and/or a nascent AGN (e.g., Barnes & Hernquist 1992). Morphological and kinematic studies of ULIRGs also suggest that their stellar populations are evolving into relaxed, elliptical-like distributions (Wright et al. 1990; Genzel et al. 2001, Tacconi et al. 2002).

Luminous Infrared Galaxies, or LIRGs (those galaxies with $L_{\rm IR} \geq 10^{11}\ L_{\odot}$), are interesting phenomena in their own right, but they also may play a central role in our understanding of the general evolution of galaxies and black holes, as demonstrated by two key observational results. First, observations with ISO and *Spitzer* have shown that LIRGs comprise a significant fraction ($\geq 50\%$) of the cosmic infrared background and dominate the star-formation activity at $z \sim 1$ (Elbaz et al. 2002; Le Floch et al. 2005; Caputi et al. 2007, Magnelli et al. 2009). In comparison to the local universe where they are relatively rare, ULIRGs are about a thousand times more common at $z \gtrsim 2$ (Blain et al. 2002; Chapman et al. 2005). Second, the ubiquity of supermassive nuclear black holes in quiescent galaxies and the scaling of their masses with stellar bulge masses (Magorrian et al. 1998; Ferrarese & Merritt 2000; Gebhardt et al. 2000) suggest an intimate connection between the evolution of massive galaxies and their central black holes. One explanation for the relationship is that mass accretion onto the black hole occurs during episodes of nuclear star formation. The study of a large, complete sample of local LIRGs spanning all merger and interaction stages can shed critical light on the coevolution of black holes and stellar bulges in massive galaxies.

The Great Observatories All-Sky LIRG Survey (GOALS) combines data from NASA's *Spitzer, HST, Chandra,* and *GALEX* observatories in a comprehensive imaging and spectroscopic survey of over 200 low-redshift ($z < 0.088$) LIRGs (see Table 1). The primary new data sets consist of *Spitzer* Infrared Array Camera (IRAC) and Multi-band Imaging Photometer for Spitzer (MIPS) imaging; Infrared Spectrograph (IRS) spectroscopy (Houck et al. 2004); *HST* Advanced Camera for Surveys (ACS), Near Infrared Camera and Multi-Object Spectrometer (NICMOS), and Wide Field and Planetary Camera 2 (WFPC2) imaging; *Chandra* AXAF CCD Imaging Spectrometer (ACIS) imaging; and *GALEX* far and near-UV observations. The majority of the new observations are being led by GOALS team members, but we also make use of the *Spitzer, HST, Chandra,* and *GALEX* archives to fill out the sample data (see Table 2). In addition, optical and K-band imaging (Ishida et al. 2004); optical spectra (Kim et al. 1995); J, H, and K_s-band near-infrared images from 2MASS (Skrutskie et al. 2006); submillimeter images (Dunne et al. 2000); CO and HCN (Sanders et al. 1991; Gao & Solomon 2004); and 20 cm VLA imaging (Condon et al. 1990) exist for various subsets of the LIRGs in GOALS, in addition to the IRAS data with which the sources were selected (Sanders et al. 2003). In this article we introduce the main components of the survey, present our primary science objectives, and discuss the multiwavelength results for one source, VV 340. The layout of the paper is as follows. The scientific objectives are discussed in § 2, followed by a definition of the sample in § 3. In § 4 we describe the observations, in § 5 we outline the *Spitzer* Legacy data products being delivered, and in § 6 we present results for the LIRG VV 340.

2. SCIENTIFIC OBJECTIVES OF GOALS

While a great deal of effort has been devoted to the study of ULIRGs, LIRGs have, in comparison, suffered from a lack of attention. Ground-based optical and near-infrared imaging studies of low-redshift LIRGs have been performed (e.g., Ishida 2004), but multiwavelength imaging and spectroscopic surveys of a large sample of the nearest and brightest LIRGs have not been completed. This is undoubtedly due to the fact that LIRGs form a morphologically diverse group of galaxies, unlike ULIRGs which are nearly always involved in the final stages of a violent and spectacular merger. LIRGs are also much harder to detect and analyze at high redshift in many shallow surveys, which has traditionally removed much of the impetus behind establishing a robust library of low-redshift analogs. This has changed recently, with surveys such as COSMOS (Scoville et al. 2007) and GOODS (Dickinson et al. 2003), which include significant samples of LIRGs at cosmologically interesting epochs.

An important question regarding the nature of LIRGs is, what is the source of their power? What mechanism is responsible for generating energy at a rate that is tens to hundreds of times larger than that emitted by a typical galaxy? Interactions between large, late-type galaxies are evident in many systems, but a significant fraction of LIRGs show no morphological evidence (e.g., double nuclei, tidal tails, stellar bridges, etc.) for a major merger. Large molecular gas masses, large gas fractions,

TABLE 1
THE GOALS SAMPLE

IRAS Name (1)	Optical ID (2)	R.A. J2000 (3)	Decl. J2000 (4)	$V_{\rm Helio}$ (km s^{-1}) (5)	D_L (Mpc) (6)	$\log(L_{ir}/L_{\odot})$ (7)
F00073+2538	NGC 0023	00 h09 m53.41 s	+25 d55 m25.6 s	4566	65.2	11.12
F00085−1223	NGC 0034	00 h11 m06.55 s	−12 d06 m26.3 s	5881	84.1	11.49
F00163−1039	Arp 256	00 h18 m50.51 s	−10 d22 m09.2 s	8159	117.5	11.48
F00344−3349	ESO 350-IG 038	00 h36 m52.25 s	−33 d33 m18.1 s	6175	89.0	11.28
F00402−2349	NGC 0232	00 h42 m45.82 s	−23 d33 m40.9 s	6647	95.2	11.44
F00506+7248	MCG +12-02-001	00 h54 m03.61 s	+73 d05 m11.8 s	4706	69.8	11.50
F00548+4331	NGC 0317B	00 h57 m40.45 s	+43 d47 m32.1 s	5429	77.8	11.19
F01053−1746	IC 1623	01 h07 m47.18 s	−17 d30 m25.3 s	6016	85.5	11.71
F01076−1707	MCG −03-04-014	01 h10 m08.96 s	−16 d51 m09.8 s	10040	144.0	11.65
F01159−4443	ESO 244-G012	01 h18 m08.15 s	−44 d27 m51.2 s	6307	91.5	11.38
F01173+1405	CGCG 436-030	01 h20 m02.72 s	+14 d21 m42.9 s	9362	134.0	11.69
F01325−3623	ESO 353-G020	01 h34 m51.28 s	−36 d08 m14.0 s	4797	68.8	11.06
F01341−3735	RR 032	01 h36 m23.79 s	−37 d19 m51.7 s	5191	74.6	11.16
F01364−1042	.....	01 h38 m52.92 s	−10 d27 m11.4 s	14464	210.0	11.85:
F01417+1651	III Zw 035	01 h44 m30.45 s	+17 d06 m05.0 s	8375	119.0	11.64:
F01484+2220	NGC 0695	01 h51 m14.24 s	+22 d34 m56.5 s	9735	139.0	11.68
F01519+3640	UGC 01385	01 h54 m53.79 s	+36 d55 m04.6 s	5621	79.8	11.05:
F02071−1023	NGC 0838	02 h09 m38.58 s	−10 d08 m46.3 s	3851	53.8	11.05:
F02070+3857	NGC 0828	02 h10 m09.57 s	+39 d11 m25.3 s	5374	76.3	11.36
F02114+0456	IC 0214	02 h14 m05.59 s	+05 d10 m23.7 s	9061	129.0	11.43
F02152+1418	NGC 0877	02 h17 m59.64 s	+14 d32 m38.6 s	3913	54.6	11.10
F02203+3158	MCG +05-06-036	02 h23 m21.99 s	+32 d11 m49.5 s	10106	145.0	11.64
F02208+4744	UGC 01845	02 h24 m07.98 s	+47 d58 m11.0 s	4679	67.0	11.12
F02281−0309	NGC 0958	02 h30 m42.83 s	−02 d56 m20.4 s	5738	80.6	11.20
F02345+2053	NGC 0992	02 h37 m25.49 s	+21 d06 m03.0 s	4141	58.0	11.07
F02401−0013	NGC 1068	02 h42 m40.71 s	−00 d00 m47.8 s	1137	15.9	11.40
F02435+1253	UGC 02238	02 h46 m17.49 s	+13 d05 m44.4 s	6560	92.4	11.33:
F02437+2122	.....	02 h46 m39.15 s	+21 d35 m10.3 s	6987	98.8	11.16:
F02512+1446	UGC 02369	02 h54 m01.78 s	+14 d58 m24.9 s	9558	136.0	11.67
F03117+4151	UGC 02608	03 h15 m01.42 s	+42 d02 m09.4 s	6998	100.0	11.41
F03164+4119	NGC 1275	03 h19 m48.16 s	+41 d30 m42.1 s	5264	75.0	11.26
F03217+4022	.....	03 h25 m05.38 s	+40 d33 m29.0 s	7007	100.0	11.33
F03316−3618	NGC 1365	03 h33 m36.37 s	−36 d08 m25.4 s	1636	17.9	11.00
F03359+1523	.....	03 h38 m46.70 s	+15 d32 m55.0 s	10613	152.0	11.55:
F03514+1546	CGCG 465-012	03 h54 m16.08 s	+15 d55 m43.4 s	6662	94.3	11.20:
03582+6012	.....	04 h02 m32.48 s	+60 d20 m40.1 s	8997	131.0	11.43:
F04097+0525	UGC 02982	04 h12 m22.45 s	+05 d32 m50.6 s	5305	74.9	11.20
F04118−3207	ESO 420-G013	04 h13 m49.69 s	−32 d00 m25.1 s	3570	51.0	11.07
F04191−1855	ESO 550-IG 025	04 h21 m20.02 s	−18 d48 m47.6 s	9621	138.5	11.51
F04210−4042	NGC 1572	04 h22 m42.81 s	−40 d36 m03.3 s	6111	88.6	11.30
04271+3849	.....	04 h30 m33.09 s	+38 d55 m47.7 s	5640	80.8	11.11:
F04315−0840	NGC 1614	04 h33 m59.85 s	−08 d34 m44.0 s	4778	67.8	11.65
F04326+1904	UGC 03094	04 h35 m33.83 s	+19 d10 m18.2 s	7408	106.0	11.41
F04454−4838	ESO 203-IG001	04 h46 m49.50 s	−48 d33 m32.9 s	15862	235.0	11.86:
F04502−3304	MCG −05-12-006	04 h52 m04.96 s	−32 d59 m25.6 s	5622	81.3	11.17
F05053−0805	NGC 1797	05 h07 m44.88 s	−08 d01 m08.7 s	4441	63.4	11.04
F05054+1718	CGCG 468-002	05 h08 m20.5 s	+17 d21 m58 s	5454	77.9	11.22
05083+2441	.....	05 h11 m25.88 s	+24 d45 m18.3 s	6915	99.2	11.26:
F05081+7936	VII Zw 031	05 h16 m46.44 s	+79 d40 m12.6 s	16090	240.0	11.99
05129+5128	.....	05 h16 m56.10 s	+51 d31 m56.5 s	8224	120.0	11.42
F05189−2524	.....	05 h21 m01.47 s	−25 d21 m45.4 s	12760	187.0	12.16
F05187−1017	.....	05 h21 m06.54 s	−10 d14 m46.7 s	8474	122.0	11.30:
05223+1908	.....	05 h25 m16.50 s	+19 d10 m46.0 s	8867	128.0	11.65:
05368+4940	MCG +08-11-002	05 h40 m43.71 s	+49 d41 m41.5 s	5743	83.7	11.46
F05365+6921	NGC 1961	05 h42 m04.65 s	+69 d22 m42.4 s	3934	59.0	11.06
F05414+5840	UGC 03351	05 h45 m47.88 s	+58 d42 m03.9 s	4455	65.8	11.28
05442+1732	.....	05 h47 m11.18 s	+17 d33 m46.7 s	5582	80.5	11.30

TABLE 1 (*Continued*)

IRAS Name (1)	Optical ID (2)	R.A. J2000 (3)	Decl. J2000 (4)	$V_{\rm Helio}$ (km s^{-1}) (5)	D_L (Mpc) (6)	$\log(L_{ir}/L_{\odot})$ (7)
F06076−2139	.....	06 h09 m45.81 s	−21 d40 m23.7 s	11226	165.0	11.65
F06052+8027	UGC 03410	06 h14 m29.63 s	+80 d26 m59.6 s	3921	59.7	11.10:
F06107+7822	NGC 2146	06 h18 m37.71 s	+78 d21 m25.3 s	893	17.5	11.12
F06259−4708	ESO 255-IG007	06 h27 m22.45 s	−47 d10 m48.7 s	11629	173.0	11.90
F06295−1735	ESO 557-G002	06 h31 m47.22 s	−17 d37 m17.3 s	6385	93.6	11.25
F06538+4628	UGC 3608	06 h57 m34.45 s	+46 d24 m10.8 s	6401	94.3	11.34
F06592−6313	.....	06 h59 m40.25 s	−63 d17 m52.9 s	6882	104.0	11.24
F07027−6011	AM 0702-601	07 h03 m26.37 s	−60 d16 m03.7 s	9390	141.0	11.64
07063+2043	NGC 2342	07 h09 m18.08 s	+20 d38 m09.5 s	5276	78.0	11.31:
F07160−6215	NGC 2369	07 h16 m37.73 s	−62 d20 m37.4 s	3240	47.6	11.16
07251−0248	.....	07 h27 m37.55 s	−02 d54 m54.1 s	26249	400.0	12.39:
F07256+3355	NGC 2388	07 h28 m53.44 s	+33 d49 m08.7 s	4134	62.1	11.28:
F07329+1149	MCG +02-20-003	07 h35 m43.37 s	+11 d42 m33.5 s	4873	72.8	11.13:
08355−4944	.....	08 h37 m01.82 s	−49 d54 m30.2 s	7764	118.0	11.62
F08339+6517	.....	08 h38 m23.18 s	+65 d07 m15.2 s	5730	86.3	11.11
F08354+2555	NGC 2623	08 h38 m24.08 s	+25 d45 m16.6 s	5549	84.1	11.60
08424−3130	ESO 432-IG006	08 h44 m28.07 s	−31 d41 m40.6 s	4846	74.4	11.08
F08520−6850	ESO 060-IG 016	08 h52 m31.29 s	−69 d01 m57.0 s	13885	210.0	11.82:
F08572+3915	.....	09 h00 m25.39 s	+39 d03 m54.4 s	17493	264.0	12.16
09022−3615	.....	09 h04 m12.70 s	−36 d27 m01.1 s	17880	271.0	12.31
F09111−1007	.....	09 h13 m37.61 s	−10 d19 m24.8 s	16231	246.0	12.06
F09126+4432	UGC 04881	09 h15 m55.11 s	+44 d19 m54.1 s	11851	178.0	11.74
F09320+6134	UGC 05101	09 h35 m51.65 s	+61 d21 m11.3 s	11802	177.0	12.01:
F09333+4841	MCG +08-18-013	09 h36 m37.19 s	+48 d28 m27.7 s	7777	117.0	11.34
F09437+0317	Arp 303	09 h46 m20.71 s	+03 d03 m30.5 s	5996	92.9	11.23:
F10015−0614	NGC 3110	10 h04 m02.11 s	−06 d28 m29.2 s	5054	79.5	11.37:
F10038−3338	ESO 374-IG 032[a]	10 h06 m04.8 s	−33 d53 m15.0 s	10223	156.0	11.78
F10173+0828	.....	10 h20 m00.21 s	+08 d13 m33.8 s	14716	224.0	11.86
F10196+2149	NGC 3221	10 h22 m19.98 s	+21 d34 m10.5 s	4110	65.7	11.09
F10257−4339	NGC 3256	10 h27 m51.27 s	−43 d54 m13.8 s	2804	38.9	11.64
F10409−4556	ESO 264-G036	10 h43 m07.67 s	−46 d12 m44.6 s	6299	100.0	11.32
F10567−4310	ESO 264-G057	10 h59 m01.79 s	−43 d26 m25.7 s	5156	83.3	11.14:
F10565+2448	.....	10 h59 m18.14 s	+24 d32 m34.3 s	12921	197.0	12.08
F11011+4107	MCG +07-23-019	11 h03 m53.20 s	+40 d50 m57.0 s	10350	158.0	11.62
F11186−0242	CGCG 011-076	11 h21 m12.26 s	−02 d59 m03.5 s	7464	117.0	11.43
F11231+1456	.....	11 h25 m47.30 s	+14 d40 m21.1 s	10192	157.0	11.64
F11255−4120	ESO 319-G022	11 h27 m54.08 s	−41 d36 m52.4 s	4902	80.0	11.12
F11257+5850	NGC 3690	11 h28 m32.25 s	+58 d33 m44.0 s	3093	50.7	11.93
F11506−3851	ESO 320-G030	11 h53 m11.72 s	−39 d07 m48.9 s	3232	41.2	11.17
F12043−3140	ESO 440-IG058	12 h06 m51.82 s	−31 d56 m53.1 s	6956	112.0	11.43
F12112+0305	.....	12 h13 m46.00 s	+02 d48 m38.0 s	21980	340.0	12.36:
F12116+5448	NGC 4194	12 h14 m09.47 s	+54 d31 m36.6 s	2501	43.0	11.10
F12115−4656	ESO 267-G030	12 h14 m12.84 s	−47 d13 m43.2 s	5543	97.1	11.25:
12116−5615	.....	12 h14 m22.10 s	−56 d32 m33.2 s	8125	128.0	11.65
F12224−0624	.....	12 h25 m03.91 s	−06 d40 m52.6 s	7902	125.0	11.36:
F12243−0036	NGC 4418	12 h26 m54.62 s	−00 d52 m39.2 s	2179	36.5	11.19
F12540+5708	UGC 08058	12 h56 m14.24 s	+56 d52 m25.2 s	12642	192.0	12.57
F12590+2934	NGC 4922	13 h01 m24.89 s	+29 d18 m40.0 s	7071	111.0	11.38
F12592+0436	CGCG 043-099	13 h01 m50.80 s	+04 d20 m00.0 s	11237	175.0	11.68
F12596−1529	MCG −02-33-098	13 h02 m19.70 s	−15 d46 m03.0 s	4773	78.7	11.17
F13001−2339	ESO 507-G070	13 h02 m52.35 s	−23 d55 m17.7 s	6506	106.0	11.56
13052−5711	.....	13 h08 m18.73 s	−57 d27 m30.2 s	6364	106.0	11.40:
F13126+2453	IC 0860	13 h15 m03.53 s	+24 d37 m07.9 s	3347	56.8	11.14:
13120−5453	.....	13 h15 m06.35 s	−55 d09 m22.7 s	9222	144.0	12.32
F13136+6223	VV 250a	13 h15 m35.06 s	+62 d07 m28.6 s	9313	142.0	11.81
F13182+3424	UGC 08387	13 h20 m35.34 s	+34 d08 m22.2 s	6985	110.0	11.73
F13188+0036	NGC 5104	13 h21 m23.08 s	+00 d20 m32.7 s	5578	90.8	11.27
F13197−1627	MCG −03-34-064	13 h22 m24.46 s	−16 d43 m42.9 s	4959	82.2	11.28

TABLE 1 (*Continued*)

IRAS Name (1)	Optical ID (2)	R.A. J2000 (3)	Decl. J2000 (4)	$V_{\rm Helio}$ (km s^{-1}) (5)	D_L (Mpc) (6)	$\log(L_{ir}/L_{\odot})$ (7)
F13229−2934	NGC 5135	13 h25 m44.06 s	−29 d50 m01.2 s	4105	60.9	11.30
13242−5713	ESO 173-G015	13 h27 m23.78 s	−57 d29 m22.2 s	2918	34.0	11.38:
F13301−2356	IC 4280	13 h32 m53.40 s	−24 d12 m25.7 s	4889	82.4	11.15
F13362+4831	NGC 5256	13 h38 m17.52 s	+48 d16 m36.7 s	8341	129.0	11.56
F13373+0105	Arp 240	13 h39 m55.00 s	+00 d50 m07.0 s	6778	108.5	11.62
F13428+5608	UGC 08696	13 h44 m42.11 s	+55 d53 m12.6 s	11326	173.0	12.21
F13470+3530	UGC 08739	13 h49 m13.93 s	+35 d15 m26.8 s	5032	81.4	11.15:
F13478−4848	ESO 221-IG010	13 h50 m56.94 s	−49 d03 m19.5 s	3099	62.9	11.22
F13497+0220	NGC 5331	13 h52 m16.29 s	+02 d06 m17.0 s	9906	155.0	11.66
F13564+3741	Arp 84	13 h58 m35.81 s	+37 d26 m20.3 s	3482	58.7	11.08
F14179+4927	CGCG 247-020	14 h19 m43.25 s	+49 d14 m11.7 s	7716	120.0	11.39
F14280+3126	NGC 5653	14 h30 m10.42 s	+31 d12 m55.8 s	3562	60.2	11.13
F14348−1447	.....	14 h37 m38.37 s	−15 d00 m22.8 s	24802	387.0	12.39:
F14378−3651	.....	14 h40 m59.01 s	−37 d04 m32.0 s	20277	315.0	12.23:
F14423−2039	NGC 5734	14 h45 m09.05 s	−20 d52 m13.7 s	4121	67.1	11.15:
F14547+2449	VV 340a	14 h57 m00.68 s	+24 d37 m02.7 s	10094	157.0	11.74
F14544−4255	IC 4518	14 h57 m42.82 s	−43 d07 m54.3 s	4763	80.0	11.23
F15107+0724	CGCG 049-057	15 h13 m13.09 s	+07 d13 m31.8 s	3897	65.4	11.35:
F15163+4255	VV 705	15 h18 m06.28 s	+42 d44 m41.2 s	11944	183.0	11.92
15206−6256	ESO 099-G004	15 h24 m58.19 s	−63 d07 m34.2 s	8779	137.0	11.74
F15250+3608	.....	15 h26 m59.40 s	+35 d58 m37.5 s	16535	254.0	12.08
F15276+1309	NGC 5936	15 h30 m00.84 s	+12 d59 m21.5 s	4004	67.1	11.14
F15327+2340	UGC 09913	15 h34 m57.12 s	+23 d30 m11.5 s	5434	87.9	12.28
F15437+0234	NGC 5990	15 h46 m16.37 s	+02 d24 m55.7 s	3839	64.4	11.13
F16030+2040	NGC 6052	16 h05 m13.05 s	+20 d32 m32.6 s	4739	77.6	11.09
F16104+5235	NGC 6090	16 h11 m40.70 s	+52 d27 m24.0 s	8947	137.0	11.58
F16164−0746	.....	16 h19 m11.79 s	−07 d54 m02.8 s	8140	128.0	11.62:
F16284+0411	CGCG 052-037	16 h30 m56.54 s	+04 d04 m58.4 s	7342	116.0	11.45
16304−6030	NGC 6156	16 h34 m52.55 s	−60 d37 m07.7 s	3263	48.0	11.14
F16330−6820	ESO 069-IG006	16 h38 m12.65 s	−68 d26 m42.6 s	13922	212.0	11.98
F16399−0937	.....	16 h42 m40.21 s	−09 d43 m14.4 s	8098	128.0	11.63:
F16443−2915	ESO 453-G005	16 h47 m31.06 s	−29 d21 m21.6 s	6260	100.0	11.37:
F16504+0228	NGC 6240	16 h52 m58.89 s	+02 d24 m03.4 s	7339	116.0	11.93
F16516−0948	.....	16 h54 m24.03 s	−09 d53 m20.9 s	6755	107.0	11.31:
F16577+5900	NGC 6286	16 h58 m31.38 s	+58 d56 m10.5 s	5501	85.7	11.37
F17132+5313	.....	17 h14 m20.00 s	+53 d10 m30.0 s	15270	232.0	11.96
F17138−1017	.....	17 h16 m35.79 s	−10 d20 m39.4 s	5197	84.0	11.49
F17207-0014	.....	17 h23 m21.95 s	−00 d17 m00.9 s	12834	198.0	12.46:
F17222−5953	ESO 138-G027	17 h26 m43.34 s	−59 d55 m55.3 s	6230	98.3	11.41
F17530+3447	UGC 11041	17 h54 m51.82 s	+34 d46 m34.4 s	4881	77.5	11.11
F17548+2401	CGCG 141-034	17 h56 m56.63 s	+24 d01 m01.6 s	5944	93.4	11.20
17578−0400	.....	18 h00 m31.90 s	−04 d00 m53.3 s	4210	68.5	11.48:
18090+0130	.....	18 h11 m35.91 s	+01 d31 m41.3 s	8662	134.0	11.65:
F18131+6820	NGC 6621	18 h12 m55.31 s	+68 d21 m48.4 s	6191	94.3	11.29
F18093−5744	IC 4687	18 h13 m39.63 s	−57 d43 m31.3 s	5200	81.9	11.62:
F18145+2205	CGCG 142-034	18 h16 m40.66 s	+22 d06 m46.1 s	5599	88.1	11.18
F18293-3413	.....	18 h32 m41.13 s	−34 d11 m27.5 s	5449	86.0	11.88
F18329+5950	NGC 6670	18 h33 m35.91 s	+59 d53 m20.2 s	8574	129.5	11.65
F18341-5732	IC 4734	18 h38 m25.70 s	−57 d29 m25.6 s	4680	73.4	11.35
F18425+6036	NGC6701	18 h43 m12.46 s	+60 d39 m12.0 s	3965	62.4	11.12
F19120+7320	VV 414	19 h10 m59.20 s	+73 d25 m06.3 s	7528	113.0	11.49
F19115-2124	ESO 593-IG008	19 h14 m30.90 s	−21 d19 m07.0 s	14608	222.0	11.93
F19297-0406	.....	19 h32 m21.25 s	−03 d59 m56.3 s	25701	395.0	12.45:
19542+1110	.....	19 h56 m35.44 s	+11 d19 m02.6 s	19473	295.0	12.12:
F19542-3804	ESO 339-G011	19 h57 m37.54 s	−37 d56 m08.4 s	5756	88.6	11.2
F20221-2458	NGC 6907	20 h25 m06.65 s	−24 d48 m33.5 s	3190	50.1	11.11
20264+2533	MCG +04-48-002	20 h28 m35.06 s	+25 d44 m00.0 s	4167	64.2	11.11
F20304-0211	NGC 6926	20 h33 m06.11 s	−02 d01 m39.0 s	5880	89.1	11.32

TABLE 1 (*Continued*)

IRAS Name (1)	Optical ID (2)	R.A. J2000 (3)	Decl. J2000 (4)	$V_{\rm Helio}$ (km s^{-1}) (5)	D_L (Mpc) (6)	$\log(L_{ir}/L_{\odot})$ (7)
20351+2521	.....	20 h37 m17.72 s	+25 d31 m37.7 s	10102	151.0	11.61
F20550+1655	CGCG 448-020	20 h57 m23.90 s	+17 d07 m39.0 s	10822	161.0	11.94
F20551-4250	ESO 286-IG019	20 h58 m26.79 s	−42 d39 m00.3 s	12890	193.0	12.06
F21008-4347	ESO 286-G035	21 h04 m11.18 s	−43 d35 m33.0 s	5205	79.1	11.20:
21101+5810	.....	21 h11 m30.40 s	+58 d23 m03.2 s	11705	174.0	11.81:
F21330-3846	ESO 343-IG013	21 h36 m10.83 s	−38 d32 m37.9 s	5714	85.8	11.14
F21453-3511	NGC 7130	21 h48 m19.50 s	−34 d57 m04.7 s	4842	72.7	11.42
F22118-2742	ESO 467-G027	22 h14 m39.92 s	−27 d27 m50.3 s	5217	77.3	11.08
F22132-3705	IC 5179	22 h16 m09.10 s	−36 d50 m37.4 s	3422	51.4	11.24
F22287-1917	ESO 602-G025	22 h31 m25.48 s	−19 d02 m04.1 s	7507	110.0	11.34
F22389+3359	UGC 12150	22 h41 m12.26 s	+34 d14 m57.0 s	6413	93.5	11.35
F22467-4906	ESO 239-IG002	22 h49 m39.87 s	−48 d50 m58.1 s	12901	191.0	11.84
F22491-1808	.....	22 h51 m49.26s	−17 d52 m23.5 s	23312	351.0	12.20:
F23007+0836	NGC 7469	23 h03 m15.62 s	+08 d52 m26.4 s	4892	70.8	11.65
F23024+1916	CGCG 453-062	23 h04 m56.53 s	+19 d33 m08.0 s	7524	109.0	11.38:
F23128-5919	ESO 148-IG002	23 h15 m46.78 s	−59 d03 m15.6 s	13371	199.0	12.06
F23135+2517	IC 5298	23 h16 m00.70 s	+25 d33 m24.1 s	8221	119.0	11.60
F23133-4251	NGC 7552	23 h16 m10.77 s	−42 d35 m05.4 s	1608	23.5	11.11
F23157+0618	NGC 7591	23 h18 m16.28 s	+06 d35 m08.9 s	4956	71.4	11.12
F23157-0441	NGC 7592	23 h18 m22.20 s	−04 d24 m57.6 s	7328	106.0	11.40
F23180-6929	ESO 077-IG014	23 h21 m04.53 s	−69 d12 m54.2 s	12460	186.0	11.76
F23254+0830	NGC 7674	23 h27 m56.72 s	+08 d46 m44.5 s	8671	125.0	11.56
23262+0314	NGC 7679	23 h28 m46.66 s	+03 d30 m41.1 s	5138	73.8	11.11
F23365+3604	.....	23 h39 m01.27 s	+36 d21 m08.7 s	19331	287.0	12.20:
F23394-0353	MCG −01-60-022	23 h42 m00.85 s	−03 d36 m54.6 s	6966	100.0	11.27
23436+5257	.....	23 h46 m05.58 s	+53 d14 m00.6 s	10233	149.0	11.57:
F23444+2911	Arp 86	23 h47 m01.70 s	+29 d28 m16.3 s	5120	73.6	11.07
F23488+1949	NGC 7771	23 h51 m24.88 s	+20 d06 m42.6 s	4277	61.2	11.40
F23488+2018	MRK 0331	23 h51 m26.80 s	+20 d35 m09.9 s	5541	79.3.	11.50

NOTE.—Column (1): Original IRAS source, where an "F" prefix indicates the Faint Source Catalog and no prefix indicates the Point Source Catalog. Column (2): Optical cross-identification, where available from NED. For many cases where the IRAS source corresponds to a pair of optically identified galaxies, we adopt the system name instead of pair components. For example, IRAS $\rm F00163-1039$ is identified in GOALS as Arp 256 rather than "MCG − 02-01-051/2" as in Sanders et al. 2003. Column (3): The best available source right ascension (J2000) in NED as of 2008 October. Column (4): The best available source declination (J2000) in NED as of October. Column (5): The best available heliocentric redshift, expressed as a velocity, in NED as of 2008 October 2008. Column (6): The luminosity distance in Mpc derived by correcting the heliocentric velocity for the 3-attractor flow model of Mould et al. (2000) and adopting cosmological parameters $\rm H_0 = 70\ km\,s^{-1}$ Mpc, $\Omega_{\rm Vacuum} = 0.72$, and $\Omega_{\rm Matter} = 0.28$ based on the five-year WMAP results (Hinshaw et al. 2009), as provided by NED. Column (7): The total infrared luminosity in $\log_{10}$ Solar units computed using the flux densities reported in the RBGS and the lumiosity distances in column (6) using the formulae $L_{\rm ir}/L_{\odot} = 4\pi(D_L[m])^2(F_{\rm ir}[Wm^{-2}])/3.826\times10^{26}[Wm^{-2}]$, where $F_{\rm ir} = 1.8\times10^{-14}\{13.48f_{12\mu\rm m} + 5.16f_{25\mu\rm m} + 2.58f_{60\mu\rm m} + f_{100\mu\rm m}[Wm^{-2}]\}$ (Sanders & Mirabel 1996); colons indicate uncertain IRAS measurements (Sanders et al. 2003).

[a] When the IRAS Revised Bright Galaxy Sample (RBGS, Sanders et al. 2003) was compiled, IRAS $\rm F10038-3338$ was mistakenly cross-identified with the optical source IC 2545. The proper optical counterpart is ESO 374-IG 032. (See the Essential Notes in NED.)

or unusual dynamics may all play a role. Regardless of the trigger, an AGN or an intense starburst is often invoked as the most likely source of the energy in LIRGs. The relative importance of AGN and starburst activity within individual systems, for the generation of far-infrared radiation from LIRGs as a class, and how the dominant energy source changes as a function of merger stage, are important questions that can only be answered by studying a large, unbiased sample at a wide variety of wavelengths. This is the primary motivation behind the GOALS project.

By their very nature, LIRGs are dusty galaxies, wherein a large fraction (over 90% for the most luminous systems) of the UV light emitted by stars and/or AGN is absorbed by grains and reradiated in the far-infrared. This makes traditonal UV and optical spectroscopic techniques for detecting and measuring starbursts and AGN (e.g., emission-line ratios and line widths)

TABLE 2
GOALS DATA SETS

Type (1)	Wavelength/Filter (2)	Observatory (3)	Number (4)
X-Ray Imaging & Spectroscopy	04–7 keV	Chandra–ACIS	44
Ultraviolet imaging	1528 Å(FUV), 2271 Å(NUV)	GALEX	124
Ultraviolet imaging	1400 Å(F140LP)	Hubble–ACS/SBC	30
Ultraviolet imaging	2180 Å(F218W)	Hubble–WFPC2	30
Visual imaging	4350 Å(F435W), 8140 Å(F814W)	Hubble–ACS	88
Near-Infrared imaging	16 μm (F160W)	Hubble–NICMOS	88
Mid-Infrared imaging	3.6, 4.5, 5.4, 8 μm	Spitzer–IRAC	202
Mid-Infrared nuclear spectroscopy	5–40 μm low-res, 10–40 μm high-res	Spitzer–IRS	202
Mid-Infrared spectral mapping	5–40 μm low-res	Spitzer–IRS	42
Far-Infrared imaging	24,70,160 μm	Spitzer–MIPS	202

NOTE.—Summary of the primary (Spitzer, Chandra, Hubble, and GALEX) GOALS data sets. The type of data, the wavelengths covered, the observatory, and the number of LIRGs (systems) observed (including archival data) are given in cols. 1–4, respectively. Ancillary data is discussed in the text.

difficult to link quantitatively to the ultimate source of the IR emission. However, by combining these data with observations in the infrared, hard x-ray, and radio, it is possible to penetrate the dust and better understand the LIRG engine.

With the *IRAS* data we have been able to construct unbiased, flux-limited samples of LIRGs and measure their global far-infrared colors, albeit with little or no information about the distribution of the dust, due to the large *IRAS* beam sizes. The overall LIRG Spectral Energy Distributions (SEDs) are shaped by the relative locations of the dust and the young stars, as well as the presence of an active nucleus. At a basic level, the size of the warm dust-emitting region can give an indication of the power source, as a starburst will be spread out on kpc scales while the region heated by an AGN will be 2–3 orders of magnitude smaller. *Spitzer* imaging with IRAC and MIPS can give us our first estimates of the size of the IR-emitting regions in the nearest LIRGs, although higher spatial resolution is required for the vast majority of systems if we are to place meaningful constraints on, for example, the luminosity density of the nuclear starburst. Ground-based 10–20 μm imaging can provide a high spatial resolution view of the nucleus, but these wavelengths are most sensitive to the hottest dust, and extrapolations to the far-infrared are always required. The IRAC data provide the finest spatial resolution on *Spitzer*, and as the IRAC bands for low-redshift galaxies are dominated by stars, hot dust, and finally polycyclic aromatic hydrocarbon (PAH) emission as one progresses from 3.6 μm to 8 μm, the nuclear colors themselves can indicate the presence of an AGN (Lacy et al. 2004; Stern et al. 2005). Although the spatial resolution of the MIPS data is limited, the flux ratios give an indication of the dust temperature and hence, the importance of an AGN to the overall energy budget. When coupled with the radio continuum data, the MIPS fluxes can also be used to estimate the radio–far-infrared flux ratio, itself an indicator of the presence of a (radio loud) AGN.

Mid-infrared and X-ray spectroscopy provide powerful tools for not only uncovering buried AGN, but also measuring the physical properties of the gas and dust surrounding the central source. The low-resolution IRS spectra are ideal for measuring the broad PAH features at 6.2, 7.7, 8.6, 11.3, and 12.7 μm; the silicate absorption features at 9.7 and 18 μm; and water or hydrocarbon ices at 5–7 μm (e.g., Spoon et al. 2004; Armus et al. 2007). The PAH ratios indicate the size and ionization state of the small grains (e.g., Draine & Li 2001), while the silicate absorption gives a direct measure of the optical depth toward the nuclei and clues as to the geometry of the obscuring medium (e.g., Levenson et al. 2007, Sirocky et al. 2008). The ratio of the PAH emission to the underlying (hot dust) continuum can be used as a measure of the strength of an AGN, as Seyert galaxies and quasars typically have extremely low PAH equivalent widths (EQW) compared to starburst galaxies (Genzel et al. 1998; Sturm et al. 2002; Armus et al. 2004, 2006, 2007). Among ULIRGs, the PAH EQW have even been shown to decrease with increasing luminosity (Tran et al. 2001; Desai et al. 2007), suggesting an increasing importance of an AGN in the highest luminosity systems. Since the strengths of the PAH features can dominate broadband, mid-infrared filter photometry, it is critical to understand how the relative strengths of the PAH features vary within the LIRG population and how they affect the colors with redshift (see Armus et al. 2007). In addition, the shape of the silicate absorption can indicate the presence of crystalline silicates, themselves a clear sign of violent, and recent, grain processing (e.g., Spoon et al. 2006).

The high-resolution IRS spectra are ideally suited for measuring the equivalent widths and relative line strengths of the narrow, fine-structure atomic emission lines such as [S IV] 10.5 μm, [Ne II] 12.8 μm, [Ne III] 15.5 μm, [Ne V] 14.3 and 24.3 μm, [O IV] 25.9 μm, [S III] 18.7 and 33.5 μm, [Si II] 34.8 μm, [Fe II] 17.9 and 25.9 μm, as well as the pure rotational H_2 lines at 9.66 μm, 12.1 μm, 17.0 μm, and 28.2 μm. These lines provide a sensitive measure of the ionization state and density of the gas, and they can be also used to infer the basic properties (e.g., $T_{\rm eff}$) of the young stellar population.

The H_2 lines probe the warm (100–500 K) molecular gas and, when combined with measurements of the cold molecular gas via the mm CO line, can be used to infer the warm-to-cold molecular gas fraction as a function of evolutionary state (e.g., Higdon et al. 2007). The high-resolution spectra can also indicate the presence of a warm, interstellar medium, via absorption features of C_2H_2 and HCN at 13.7 μm and 14.0 μm, respectively (see Lahuis et al. 2007).

The low background of the ACIS detector, together with the excellent spatial resolution of *Chandra*, provide an unprecedented view of the 0.4–8 keV X-ray emission in LIRGs. X-ray binaries, an AGN, and hot gas associated with an outflowing wind can all contribute to the measured X-ray emission on different physical scales and at different characteristic energies. The X-ray images will allow us to quantify the amount and extent of resolved X-ray emission in LIRGs as an indication of extent of the starburst, and/or the presence of an outflowing wind. The winds are driven through the combined action of overlapping supernovae, producing both a hot central component and soft, extended emission, made up predominantly of shocked, swept-up gas in the ISM (e.g., Fabbiano et al. 1990; Heckman et al. 1990; Armus et al. 1995; Read et al. 1997; Dahlem et al. 1998; Strickland et al. 2004a, 2004b). An AGN, on the other hand, will produce unresolved hard X-ray emission, sometimes accompanied by a strong neutral or ionized iron line.

The penetrating power of the hard X-rays implies that even obscured AGN should be visible to *Chandra* (e.g., Komossa et al. 2003). Unresolved, hard X-ray (2–8 keV) flux with strong iron line emission is a clear indication of an AGN, and by fitting the spectrum we can derive both the intrinsic luminosity and the HI column toward the accretion disk(s). Of course, identifying the true nature of the nuclear emission from the *Chandra* spectra alone is difficult for sources where the HI column density exceeds $\sim 10^{24}$ cm^{-2}, but the combination of X-ray spectral and spatial information can help disentangle the extended starburst emission from the unresolved, harder emission from an AGN in many LIRGs. Of particular interest among the LIRG sample is whether or not the X-ray luminosity can be used as a quantitative measure of the star-formation rate. In galaxies dominated by star formation, where the X-ray emission is dominated by high-mass X-ray binaries, there is a correlation between the X-ray luminosity and the star-formation rate as measured by the infrared or radio emission (Ranalli et al. 2003; Grimm et al. 2003). It will be interesting to determine whether or not this relation holds for the powerful starbursts found in LIRGs.

The radio emission from galaxies is immune to the effects of dust obscuration, and the far-infrared to radio flux ratio, q (Helou et al. 1985), shows a tight correlation for star-forming galaxies (Yun et al. 2001). In addition, the radio spectral index and the radio morphology can be used to identify buried AGN and/or jets in the nuclei of LIRGs at the high spatial resolution afforded with the VLA. The available GHz radio data for the GOALS sample (Condon et al. 1990) will therefore provide a critical baseline for understanding the power sources and the ISM properties of the GOALS sample. In particular, it will be valuable to compare the radio and far-infrared morphologies of the nearest LIRGs and explore the far-infrared–radio correlation in detail within luminous infrared galaxies, such has been done for other nearby samples (e.g., Murphy et al. 2006).

In addition to uncovering buried AGN and nuclear starbursts in LIRGs, GOALS provides an excellent opportunity to study star formation in LIRG disks as a function of merger stage. The wide wavelength coverage and sensitivity provide a detailed look at the old and young stars, the dust, and the gas across the merger sequence. GOALS will allow us to answer some important questions about galactic mergers, such as, what fraction of the star formation occurs in extranuclear (super) star clusters? Can the ages and locations of these clusters be used to reconstruct the merger history and refine detailed models of the merger process, and what are the physical processes that drive star-formation on different scales in the merger? A simple question that still needs to be addressed is the range in UV properties of LIRGs. Are LIRGs as a class, weak or strong UV emitters? How much of the ionizing flux emerges, and is the ratio of IR to UV emission related to any of the other properties, e.g., the merger state or the distribution of the dust?

GALEX has provided our first look at the properties of large numbers of UV-selected starburst and AGN as a function of cosmic epoch (e.g., Gil de Paz et al. 2007; Xu et al. 2007; Martin et al. 2007; Schiminovich et al. 2007). By combining the GALEX and Spitzer data, we will be able to make a full accounting of the energy balance throughout the GOALS sample, relating the UV emission to the infrared photometric and spectroscopic properties of a complete sample of low-redshift LIRGs. In the GOALS targets that are resolved by GALEX (a small but important subsample), we will be able to separate the nucleus and disk in single systems, and the individual galaxies in interacting systems, in order to measure the relative UV emission escaping from the systems and directly compare this to the far-infrared emission measured with *Spitzer*. This will provide a detailed look at the variation in the IR to UV ratio within interacting galaxies at all stages.

The HST imaging data in GOALS provides our sharpest look at the stellar clusters and detailed morphological features in LIRGS. The depth and high spatial resolution of the *HST* imaging with the Advanced Camera for Surveys (ACS) Wide Field Camera (WFC) allows for a sensitive search for faint remnants of past, or less-disruptive (minor) mergers (e.g., shells, fading tails, etc.), small scale nuclear bars, and even close, double nuclei, although the latter are notoriously difficult to measure at optical wavelengths in heavily obscured systems. These data will be used to fit models of galaxy surface brightness profiles with standard programs (e.g., GALFIT) and estimate basic structural parameters (e.g. bulge to disk ratio, half-light radius) for the LIRGs as a class, and as a function

of nuclear properties (e.g., AGN or starburst-dominated spectra as determined from the *Spitzer* IRS and *Chandra* data).

The subarcsec resolution of the ACS also allows a sensitive search for and quantitative measurement of the young, star-forming clusters in LIRGs. The cluster populations can be placed on color magnitude diagrams in order to estimate their ages, and the number and luminosity of such systems can be studied as a function of the relative age of the merger. Particularly powerful in studying the cluster ages will be the combination of visual and UV imaging with ACS (the latter obtained with the Solar Blind Channel, SBC) as the colors will then allow us to break the age-reddening degeneracy over a large range in cluster ages (10^6–10^8 yrs). The cluster results can then be compared to models of the interaction, as has been done in some well-studied mergers (e.g., NGC 4038/9–Whitmore & Schweizer 1995; Whitmore et al. 2005, 2007; Mengel et al. 2001, 2005). For example, it has recently been shown that while the interacting LIRG NGC 2623 possesses a large number of young star clusters that probably formed in the interaction, they account for a negligible fraction ($<1\%$) of the bolometric luminosity (Evans et al. 2008).

Our understanding of the UV emission properties of LIRGs will be greatly enhanced by the addition of the high-resolution ACS far-UV imaging data. Only a handful of LIRGs have been imaged in the vacuum ultraviolet at high resolution (e.g., Goldader et al. 2002). Although the study of the cluster populations is the primary scientific goal for the ACS imaging, they also will be extremely valuable for understanding the physical conditions that drive luminous infrared galaxies away from the well-known IRX-β correlation—the correlation between infrared excess and UV spectral slope (see Meurer et al. 1999; Goldader et al. 2002). ULIRGs fall well off the correlation established for starburst galaxies, and this is usually interpreted simply as disconnect between the sources of the observed UV and far-infrared emission caused by dust obscuration. However, the physical conditions over which this occurs and when this sets in during the merger process is not known. By combining the ACS, *GALEX,* and *Spitzer* imaging data, we will be able to greatly extend the luminosity range over which the UV (and IR) emissions have been mapped, as well as to sample galaxies along the merger sequence.

To understand the true stellar distribution in the dusty circumnuclear regions in LIRGs, it is important to combine high-resolution and long-wavelength imaging. The subarcsecond *HST* NICMOS imaging in GOALS will provide us with our clearest picture of the stellar mass in the LIRG nuclei, and allow us to accurately deredden the stellar clusters seen in the ACS data. With these data we will be able to search for very small-scale, extremely red point sources that may be buried AGN, and find secondary nuclei hidden from even the deepest ACS optical observations. In addition, we will be able to find optically faint or even invisible clusters around the nuclei, and together with the ACS data, to assemble a true cluster luminosity function unaffected by dust. The H-band imaging provides us with the best (existing) near-infrared imaging resolution, and it samples the peak in the stellar light curve for the old stars that will dominate the mass in these galaxies. While the NICMOS F160W and the IRAC 3.6 μm data are both effective tracers of the old stars and stellar mass, the NICMOS data have a spatial resolution that is an order of magnitude higher–on the order of 100 pc or better for many of the LIRGs. By combining the IRAC imaging of the entire sample with the NICMOS imaging of the luminous GOALS systems, we will be able to trace the stellar masses from the largest to the smallest scales.

A basic result from the *Spitzer* imaging in GOALS will be a much better understanding of the distribution of the dust in mergers. Since many of the LIRGs are interacting, yet not fully merged, the IRAC and MIPS images allow us to separate the contribution from each galaxy to the total far-infrared flux as measured by *IRAS*. They also allow us to separate nuclear from disk emission in many systems, pinpointing the location of the enhanced infrared luminosity as a function of merger state. The MIPS images provide a clean separation between the warm dust ($T \sim 50$–100 K) at 24 μm and 70 μm, and the cold dust, which contributes mostly at 160 μm. One of the most remarkable results from ISO was the discovery that most of the far-infrared emission in the merging galaxy NGC 4038/9 (the "Antennae") originates from the disk overlap region, which is extremely faint in the UV and optical (Mirabel et al. 1998). The *Spitzer* GOALS images will allow us to find other systems like the Antennae, and determine the frequency of this completely dust-enshrouded starburst state among the LIRG population as a whole.

Taken together, the imaging and spectroscopic data in GOALS will provide the most comprehensive look at the LIRG population in the local Universe. By studying LIRGs from the X-ray through the radio and far-infrared, we can piece together an understanding of the stars, central black holes, and the interstellar medium (ISM) in some of the most actively evolving galaxies today. These observations will be invaluable as a local library with which to interpret the limited photometric and spectroscopic information garnered from deep surveys of LIRGs at high redshift, providing an in-depth glimpse of the coevolution of starbursts and black holes at late times, and the role of feedback on the ISM of merging galaxies.

3. SAMPLE DEFINITION AND PROPERTIES

The *IRAS* Revised Bright Galaxy Sample (RBGS; Sanders et al. 2003) is a complete sample of extragalactic objects with *IRAS* $S_{60} > 5.24$ Jy, covering the full sky above a Galactic latitude of $|b| > 5$ degrees. The RBGS objects are the brightest 60 μm sources in the extragalactic sky, and as such they are the best sources for studying the far-infrared emission processes in galaxies and for comparing them with observations at other wavelengths. The 629 objects in the RBGS all have $z < 0.088$, and near-infrared properties spanning a wide range from

normal, isolated gas-rich spirals at low luminosities ($L_{IR} < 10^{10.5}\ L_{\odot}$) through an increasing fraction of interacting galaxy pairs and ongoing mergers among the more luminous LIRGs and ULIRGs. The sample includes numerous galaxies with optical nuclear spectra classified as starbursts, Type 1 and 2 Seyfert nuclei, and LINERS. The 21 ULIRGs (3%) and 181 LIRGs (29%) in the RBGS form a large, statistically complete sample of 202 infrared-luminous, local galaxies which are excellent analogs for comparisons with infrared and submm selected galaxies at high redshift. These infrared-luminous sources define a set of galaxies sufficiently large to sample each stage of interaction and provide a temporal picture of the merger process and its link to the generation of far-infrared radiation. The full sample of LIRGs, along with their basic properties, is listed in Table 1. Note that 77 of the LIRG systems contain multiple galaxies. From this point on we refer to the 202 LIRGs as "systems," comprising approximately 291 individual galaxies. The median distance to the LIRGs in the GOALS sample is 94.8 Mpc. Throughout this article we adopt $H_0 = 70\ km\,s^{-1}\,Mpc$, $\Omega_{vacuum} = 0.72$, and $\Omega_{matter} = 0.28$.

Note that an update to the cosmological parameters, primarily $H_0 = 70\ km\,s^{-1}\,Mpc$ (Hinshaw et al. 2009) instead of $H_0 = 75\ km\,s^{-1}\,Mpc$, which was used when the *IRAS* Revised Bright Galaxy Sample was compiled (RBGS; Sanders et al. 2003), results in 17 additional RBGS sources classified as LIRGs, namely: *IRAS* F01556 + 2507 (UGC 01451, $\log(L_{IR}/L_{\odot}) = 11.00$); F02072 − 1025 (NGC 0839, $\log(L_{IR}/L_{\odot}) = 11.01$); F04296 + 2923 ($\log(L_{IR}/L_{\odot}) = 11.04$); F04461−0624 (NGC 1667, $\log(L_{IR}/L_{\odot}) = 11.01$); F06142 − 2121 (IC 2163, $\log(L_{IR}/L_{\odot}) = 11.03$); NGC 2341, $\log(L_{IR}/L_{\odot}) = 11.17$); F10221 − 2318 (ESO 500-G034, $\log(L_{IR}/L_{\odot}) = 11.01$); F11122 − 2327 (NGC 3597, $\log(L_{IR}/L_{\odot}) = 11.05$); F12112 − 4659 (ESO 267-G029, $\log(L_{IR}/L_{\odot}) = 11.11$); F12351 − 4015 (NGC 4575, $\log(L_{IR}/L_{\odot}) = 11.02$); F14004 + 3244 (NGC 5433, $\log(L_{IR}/L_{\odot}) = 11.02$); F14430 − 3728 (ESO 386-G019, $\log(L_{IR}/L_{\odot}) = 11.01$); F15467 − 2914 (NGC 6000, $\log(L_{IR}/L_{\odot}) = 11.07$); F17468 + 1320 (CGCG 083-025; $\log(L_{IR}/L_{\odot}) = 11.05$); F19000 + 4040 (NGC 6745, $\log(L_{IR}/L_{\odot}) = 11.04$); F22025 + 4204 (UGC 11898, $\log(L_{IR}/L_{\odot}) = 11.02$); F22171 + 2908 (Arp 278, $\log(L_{IR}/L_{\odot}) = 11.02$). Because these galaxies were not part of the original LIRG sample drawn from the RBGS, they are not included in GOALS.

4. GOALS OBSERVATIONS

4.1. *Spitzer*

4.1.1. IRAC and MIPS Imaging

Of the 202 LIRGs in our complete sample, we have obtained images of 175 with IRAC and MIPS on the *Spitzer Space Telescope* (PID 3672, PI J. Mazzarella). The remaining 27 LIRGs have been observed through other Spitzer GTO and GO programs and are available in the archive. The LIRGs were imaged with IRAC at 3.6, 4.5, 5.8, and 8.0 μm, in high dynamic range (HDR) mode to avoid saturating the bright nuclei. This provided short (1–2 s) integrations, in addition to the longer, primary exposures. Typically, five exposures of 30 s each were used, taken in a Gaussian dither pattern. The LIRGs were imaged with MIPS at 24, 70, and 160 μm using the Photometry and Super Resolution AORs. Multiple, 3–4 s exposures were taken of each source, with two or three mapping cycles being employed at each wavelength. Total integration times at each of the three MIPS wavelengths were 48, 38, and 25 s, respectively. The IRAC and MIPS photometry and images are presented in Mazzarella et al. (2009, in preparation).

4.1.2. IRS Nuclear Spectroscopy

As part of GOALS, we have obtained IRS spectra for 158 LIRGs in Table 1 (PID 30323, PI L. Armus). Of these, 115 were observed in all four IRS modules (Short-Low, Long-Low, Short-High, and Long-High), while 43 have been observed in three or fewer IRS modules in order to complete the existing archival data and ensure complete coverage for all GOALS targets.

In all cases we have used IRS Staring Mode AORs, employing "cluster target" observations for those sources with well separated ($\Delta r > 10''$), nearby interacting companions. Among the 158 LIRGs observed, there were a total of 202 nuclei targeted. We have targeted secondary nuclei only when the flux ratio of primary to secondary nucleus (as measured in the MIPS 24 μm data) is less than or equal to five, in order to capture the spectra of the nuclei actively participating in the far-infrared emission of the system. Since we wish to build up a uniform and complete set of nuclear spectra with the IRS, we have elected to observe all sources in staring mode, even though many LIRGs are resolved to *Spitzer* (predominantly at IRAC wavelengths).

Ramp durations for all modules were selected based upon the measured IRAC and MIPS nuclear flux densities in order to deliver high signal-to-noise (S/N) spectra for all LIRGs. In all cases we have used at least two cycles per nod position along the slit, and centered the sources using high-accuracy blue IRS peak-up on a nearby 2MASS star. In order to mitigate against time-varying warm pixels and measure accurate line equivalent widths in the small high-resolution slits, we have obtained background sky observations with matched integration times in the SH and LH slits. For most sources, backgrounds for the SL and LL slits are obtained from the nonprimary order (subslit) when the primary order is on the target. However, for the 11 targets with IRAC 8 μm diameters of 2.0′ or larger, we have obtained off-source backgrounds, as is done for the high-resolution modules. After background subtraction, residual bad pixels will be removed with the IRSCLEAN software available from the SSC, and spectra will be extracted (from two-dimensional to one-dimensional) using the SPICE software. The first results from the IRS spectral survey are presented in Petric et al. (2009, in preparation).

4.1.3. IRS Spectral Mapping

In order to produce spectra of the total mid-infrared emission of the systems, and to measure variations within the LIRG disks, we are obtaining IRS low-resolution (SL + LL) spectral maps of 25 LIRGs as part of a Spitzer cycle-5 GO program (PID 50702, PI L. Armus). The target LIRGs were chosen to span a large range in morphological properties (isolated through late-stage interactions) while being well-resolved in our IRAC 8 μm images (to ensure adequate area for constructing spatially-resolved spectral maps). Distances to the mapped LIRGs range from 45.5 to 105.8 Mpc, implying projected spatial resolutions at 6 μm of 0.7 to 1.8 kpc. (3.6″, or two SL pixels). Ten of these systems have two well-separated galaxies requiring individual maps, and therefore there are 35 individual maps in the program. In addition, there are 17 LIRGs with IRS spectral mapping data in the Spitzer archive.

All LIRGs will be observed with the SL and LL slits. There are typically 25–45 steps in each SL map, and 7–13 steps in each LL map, to cover areas in both slits that are 0.5–2 square arcminutes on each source. In all cases, step sizes perpendicular to the slits are $1/2$ the width of the slit. The maps are designed to cover the main bodies of the galaxies, but not the tidal tails (for those LIRGs with tails). The SL exposures are all 60 s per position, while the LL exposures are 30 s per position. IRS peakups are not used for the mapping observations. The AORs, which include the SL and LL maps, range in time from 0.8–6.0 hr each, including overheads. The spectral cubes will be assembled, and 1D spectra extracted using the CUBISM software package available from the SSC web site (Smith et al. 2007).

4.2. *Hubble Space Telescope*

4.2.1. ACS WFC Imaging

The *HST* observations are presently composed of three campaigns. The first component consists of Advanced Camera for Surveys (ACS) observations of all 88 LIRGs with $L_{\rm IR} > 10^{11.4}\ L_{\odot}$. Many of these LIRGs have tidal structure or widely separately nuclei on scales of tens to a hundred arcseconds. Thus the Wide Field Channel (WFC), with its $202'' \times 202''$ field of view, was selected to capture the full extent of each interaction in one *HST* pointing. Each LIRG was imaged with both the F435W and F814W filters, with integration times of 20 and 10 minutes, respectively. A total of 88 orbits of ACS/WFC data were obtained (PID 10592, PI A. Evans). The ACS imaging atlas and initial photometric measurements are presented in Evans et al. (2009, in preparation).

4.2.2. NICMOS Imaging

The second *HST* campaign was designed to provide high-resolution near-infrared observations to recover nuclear structure obscured from view at optical wavelengths. Observations with the Near-Infrared Camera and Multi-Object Spectrometer (NICMOS) of 59 LIRGs in the ACS-observed sample are underway. The data are being collected using camera two (NIC2) with a field of view of $19.3'' \times 19.5''$, using the F160W filter. For most of the observations, one LIRG is observed per orbit; however, there are many cases in which the galaxy pairs are too widely separated to be observed by *HST* in a single orbit. These new data are complemented by preexisting archival NICMOS data of an additional 29 GOALS LIRGs, thus providing a complete set of NIC2/F160W observations of the 88 LIRGS in the ACS-observed sample. A total of 76 orbits of NICMOS data are being obtained (PID 11235, PI J. Surace).

4.2.3. ACS SBC Imaging

The third *HST* campaign is designed to obtain near- and far-UV data of a subset of 22 of the LIRGs previously observed with the ACS/WFC that possess the highest number of luminous star clusters within their inner 30″ (i.e., the field of view of the Solar Blind Channel, SBC, of ACS). Five of the 22 LIRG systems are in widely separated pairs that require two pointings, so there are 27 galaxies being observed in total. There are three additional LIRGs with adequate far-UV imaging in the HST archives, bringing the total number of LIRG systems in GOALS with far-UV HST data to 25. The UV observations are being obtained by using the ACS/SBC and WCPC2 Planetary Camera (PC) in combination with the F140LP (far-UV) and F218W (near-UV) filters, respectively. The program (PID 11196, PI A. Evans) consists of three orbits per galaxy, with one orbit devoted to ACS/SBC (four individual integrations in a box pattern), and two orbits devoted to WFPC2 (four individual integrations total over both orbits taken in a box pattern). A total of 81 orbits of UV imaging data are being obtained.

4.3. *Chandra*

Currently, the *Chandra* X-ray Observatory observations of the GOALS targets focuses on those LIRGs with infrared luminosity larger than $10^{11.73}\ L_{\odot}$. We observed 26 targets during the Chandra Cycle8 (PID 8700551, PI D. Sanders). The X-ray imaging observations were carried out using the ACIS-S detector in VFAINT mode with a 15 ks exposure for each target. Combined with the previously observed 18 objects from the archive, the current sample consists of 44 objects. The exposure time for the objects from the archive ranges from 10 ks to 160 ks. ESO 203-IG001 is the only galaxy that was not detected. The products available for each source are the contours of a *Chandra* full-band image overlaid onto the HST/ACS *I*-band image; X-ray images in the full (0.4–7 keV), soft (0.5–2 keV), and hard (2–7 keV) band images; azimuthally-averaged radial surface brightness profiles in the soft and hard bands; an energy spectrum when sufficient counts are available (typically more than 100 counts). Other basic information is presented in Iwasawa et al. (2009a; 2009b, in preparation), and Teng et al. (2009), including detected source counts, soft

and hard band fluxes and luminosities, the X-ray hardness ratio (as a guide of a rough estimator of the spectral shape), and a measure of spatial extension of the soft X-ray emission.

4.4. GALEX

While the LIRGs are, by definition, infrared luminous, they often do have measurable UV fluxes. In fact, due to variations in the spatial distribution of the obscuring dust, a number of well-known (U)LIRGs in GOALS (e.g., Mrk 171, Mrk 266, Mrk 231, Mrk 273, Mrk 617, and Mrk 848) were first identified as starburst galaxies and AGN by the Markarian survey of UV-excess galaxies–a spectroscopic objective-prism survey conducted years before the *IRAS* survey (e.g., see Mazzarella & Balzano 1986). Of the 202 LIRGs in GOALS, 145 have been observed with the GALEX telescope in the near-UV (2271 Å) and far-UV (1528 Å) filters. Of these, 124 have high S/N detections in both filters. Most of these images were taken as part of the All-Sky Imaging Survey (AIS) or the Nearby Galaxy Survey (NGS–see Gil de Paz et al. 2007), with 51 being observed as part of GOALS (GI1-013, PI J. Mazzarella and GI5-038, PI J. Howell). The AIS integration times are short (100 s), while the NGS and GOALS observations are long, typically a few ks in duration. Details of the GALEX observations and the UV photometry are presented in Howell et al. (2009).

5. GOALS DATA PRODUCTS

On regular, approximately six-month, intervals, *Spitzer* images and spectra will be delivered to the Spitzer Science Center and made public through their Legacy program web pages. The first delivery is now available through the Spitzer Legacy web pages at the Spitzer Science Center (http://ssc.spitzer.caltech.edu/legacy/all.html), and the Infrared Science Archive (IRSA) at the Infrared Processing and Analysis Center (http://irsa.ipac.caltech.edu). For GOALS, the delivered products include: (1) IRAC image mosaics in all four IRAC bands. Images are single-extension FITS files with a pixel scale of $0.6''$pixel^{-1}. (2) MIPS image mosaics in all three MIPS bands. Images are single-extension FITS files, with wavelength-dependent pixel scales–$1.8''$pixel^{-1} at 24 μm, $4.0''$pixel^{-1} at 70 μm, and $8.0''$pixel^{-1} at 160 μm. (3) IRS nuclear spectra in all four low and high-resolution modules. Spectra are delivered in ASCII (IPAC table) format, similar to those produced by the IRS pipelines; (4) Spatial profiles at two positions along the IRS Short-Low slit (the two nod positions), in the 8.6 μm PAH, 10 μm continuum, and 12.8 μm [Ne II] fine-structure emission line. Profiles are provided in ASCII format, in units of e^- s^{-1} for each pixel. Also included in each file are the profiles at the same wavelengths for an unresolved star. The IRAC images are corrected for "banding," "muxbleed," and "column pulldown" effects, as described in the IRAC Data Handbook. The MIPS images are corrected for latents, weak jailbars, and saturation effects, where possible. The IRAC and MIPS mosaics were constructed using MOPEX to align, resample, and combine the data. The IRS spectra are extracted from the two-dimensional BCD pipeline products using the SPICE package. A standard "point source" extraction has been used for all sources. The two nod positions and multiple exposures ("cycles") are used to remove residual cosmic rays and/or bad pixels in the spectra.

6. THE LUMINOUS INFRARED GALAXY VV 340

As an example of the utility of the multiwavelength GOALS data, we present images and spectra of the LIRG, VV 340 (*IRAS* F14547+2449; Arp 302). VV 340 consists of two large, spiral galaxies, one face-on and one edge-on, separated by approximately $40''$ (27.3 kpc). The two spirals are apparently in the early stages of a merger (Bushouse & Stanford 1992, Lo et al. 1997). This system has an infrared luminosity of 5×10^{11} $L_\odot$ (Sanders et al. 2003).

6.1. Observations and Data Reduction

IRAC observations of VV 340 were performed on 2005 July 17 (PID 3672). The data were obtained in high dynamic range mode, with a 30 s frame time and a five-position Gaussian dither pattern. MIPS observations of VV 340 were performed on 2005 January 25 (PID 3672). The data were obtained in photometry mode, using the small field size and an integration time of 3 s in all three (24, 70, 160 μm) filters. One cycle was used for 24 and 70 μm, with four cycles being used at 160 μm.

IRS observations of the two VV 340 nuclei were performed on 2007 March 17 (PID 30323). The data were obtained in staring mode, using the cluster option. A moderate accuracy blue peak-up was done on a nearby 2MASS star in order to center the IRS slits on the northern and southern nuclei. On the sky, the IRS Long-Low, Short-Low, Short-High, and Long-High slits had projected position angles of 94.1, 177.8, 134.4, and 49.5°, respectively. The Long-Low, Short-Low, Short-High and Long-High observations had ramp times of 60, 30, 120, and 240 s, respectively. The high-resolution observations also had corresponding offset sky observations with the same ramp times. The data were reduced using the S15 version of the IRS pipeline at the SSC, and the spectra were extracted using the SPICE software package using the standard point-source extraction aperture.

GALEX near-UV and far-UV observations were performed on 2005 May 19 and 2007 April 29 (PID 13), for a total of 6028 s and 3042 s, respectively. VV 340 was observed with the *Chandra X-ray Observatory* on 2006 December 17 (PID 8700551). An exposure of 14.9 ks was used, yielding 285 net counts.

HST ACS observations of VV 340 were performed on 2006 January 7 (PID 10592). The data were obtained using the WFC in ACCUM mode, in the F435W and F814W filters. Three, 420 s exposures were taken in the F435W filter and two,

360 s exposures were taken in the F814W filter using the LINE dither routine. The WFC field of view is $202 \times 202''$, and the pixel size is 0.05″. The data were run through the standard pipeline processing, which removes instrumental signatures, subtracts a dark frame, flat-fields the images, removes geometric distortion, and applies a flux calibration. Additional cosmic rays were identified and removed using the *lacos_im* and *jcrrej2.cl* routines in IRAF (Rhoads 2000; Van Dokkum 2001).

6.2. Results & Discussion

The *Chandra, GALEX, HST,* and *Spitzer* images of VV 340 are shown in Figure 1. A false-color image made from the ACS F435W and F814W data is shown in Figure 2. The thick, flaring dust lane makes VV 340 N much fainter in the UV than VV 340 S, but the disk and bulge are prominent in the IRAC images. Using the ACS images, we have detected 173 unresolved "clusters" in the VV 340 system, with most of these (159, or 92%) being in the spiral arms of VV 340 south. The apparent magnitudes range from 21–27 mag in B, with absolute magnitudes ranging from 9 to -13 mag, and $B-I$ colors of 0.5–2 mag. These colors are typical for the GOALS LIRGs as a class (Vavilkin et al. 2009, in preparation). Assuming a typical cluster mass of $10^6\ M_\odot$, the ages of these clusters are $\leq 10^8$ yr, uncorrected for reddening. As a whole, the observed clusters in VV 340 south account for 3% of the total B-band light.

The total far-infrared flux densities for the VV 340 system, as measured with MIPS, are 0.43, 9.38, and 15.73 Jy at 24, 70, and 160 μm, respectively. The northern galaxy dominates at 24, 70, and 160 μm, accounting for approximately 80%, 82%, and

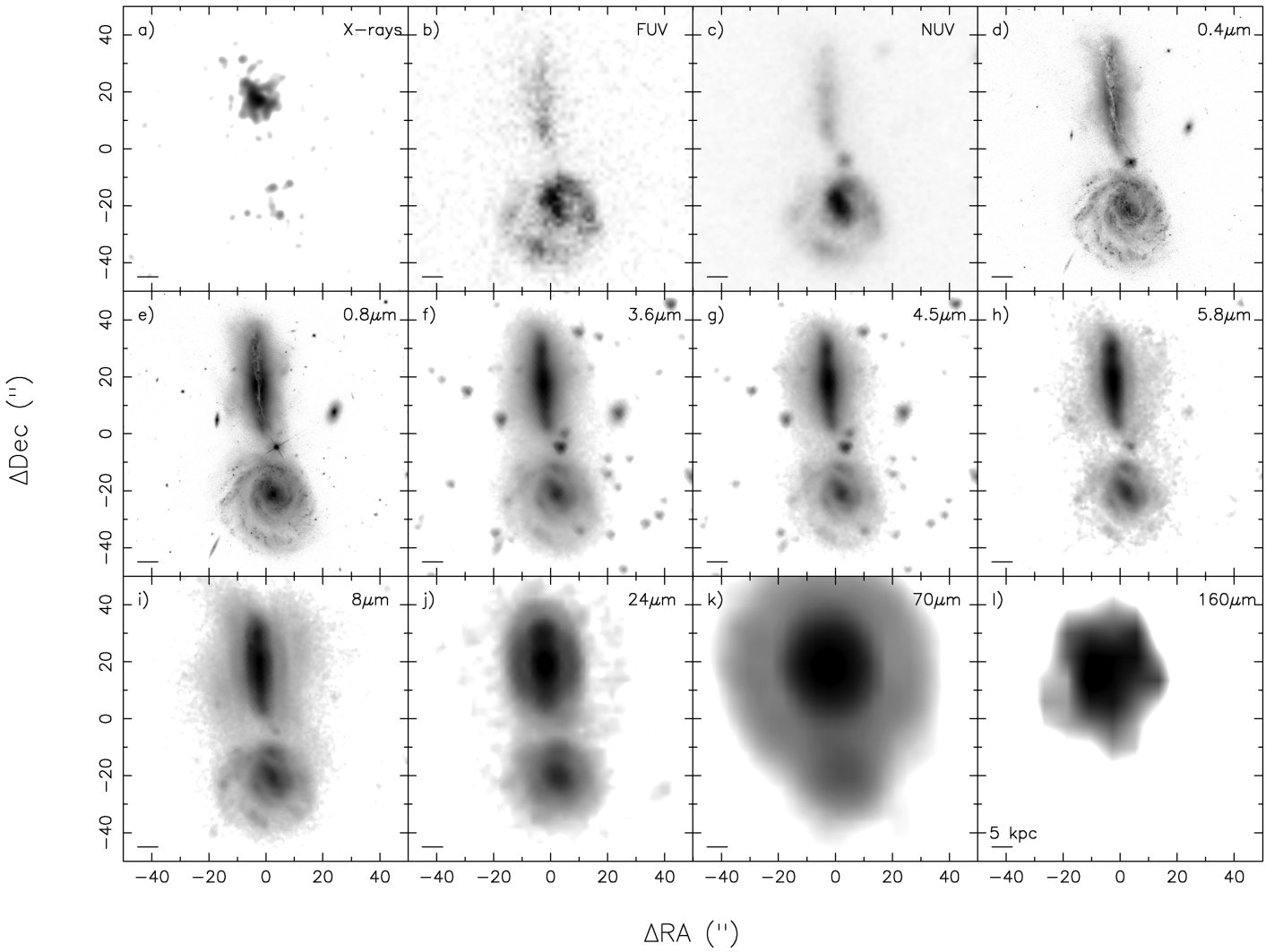

FIG. 1.—Multiwavelength images of VV 340. From upper left to lower right, these are (*a*) Chandra 0.4–8 keV, (*b*) GALEX FUV, (*c*) GALEX NUV, (*d*) HST ACS F435W, (*e*) HST ACS F814W), (*f*) Spitzer IRAC 3.6 μm, (*g*) Spitzer IRAC 4.5 μm, (*h*) Spitzer IRAC 5.8 μm, (*i*) Spitzer IRAC 8 μm., (*j*) Spitzer MIPS 24 μm, (*k*) Spitzer MIPS 70 μm, and (*l*) Spitzer MIPS 160 μm. In all cases a projected linear scale of 5 kpc at the distance of VV 340 is indicated by a bar in the lower left.

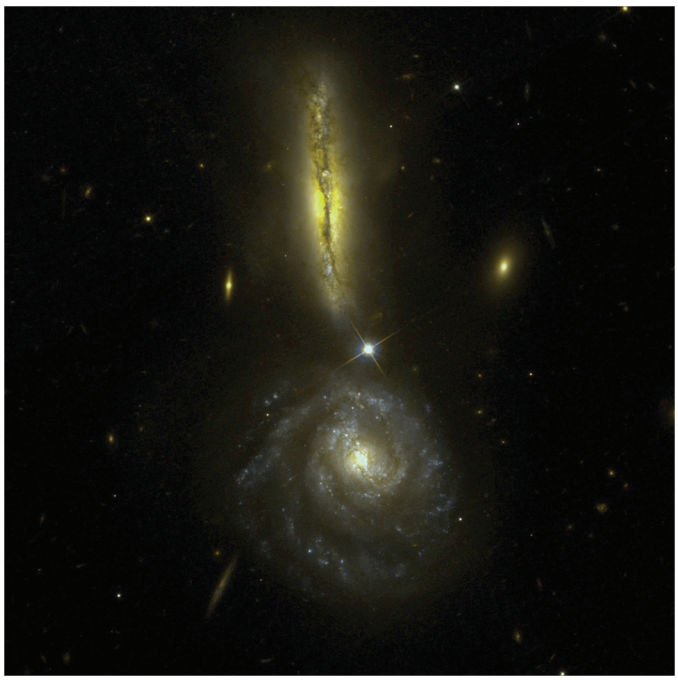

FIG. 2.—False color image of VV 340 (UGC 9618) made from the HST ACS F435W and F814W data. The image is 100″ (68 kpc) on a side. North is up and east is to the left.

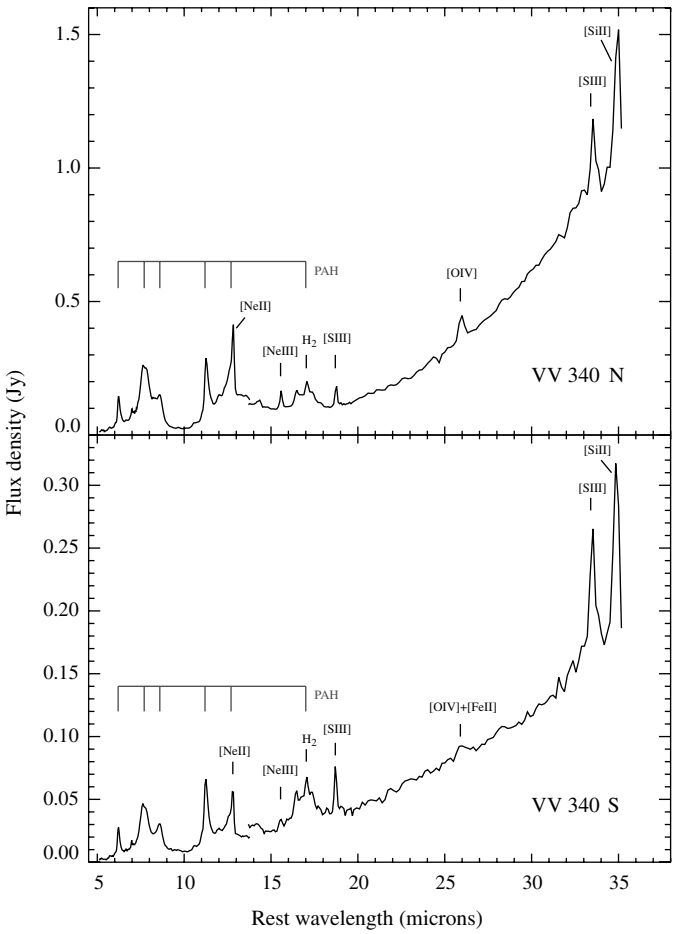

FIG. 3.—IRS low-resolution spectra of the nucleus of VV 340 north (*above*), and south (*below*). Prominent emission features are marked. The offset at 14 μm in the spectrum of VV 340 S is real, and represents a flux difference in the SL and LL spectra for this source, most likely due to significant extended emission in the LL slit.

95%, respectively, of the total emission from the system (the 160 μm ratio is uncertain because of the large size of the point-spread function, PSF). For reference, the *IRAS* 25, 60, and 100 μm flux densities for the entire VV 340 system are 0.41, 6.95, and 15.16 Jy (Sanders et al. 2003). It is interesting to note that the ratio of far-infrared fluxes implies that VV 340 south, by itself, is not a LIRG ($\log L_{\rm IR} \sim 10.71\ L_{\odot}$).

The IRAC 3.6–4.5 and 5.8–8 colors, as measured in 10 kpc radius apertures centered on the two nuclei, are 0.19 and 1.97 mag for VV 340 north, and 0.04 and 1.96 mag for VV 340 south, respectively. The nuclear (2 kpc radius aperture) colors are slightly redder, being 0.29 and 2.06 mag for VV 340 north, and 0.06 and 2.16 mag for VV 340 south, respectively. Both the large and small aperture measurements place both galaxies in VV 340 outside of the AGN "wedge" in the IRAC color-color diagram of Stern et al. (2005).

The *Spitzer* IRS low-resolution spectra of the northern and southern nuclei are shown in Figure 3. VV 340 N has a steeper spectrum and a deeper silicate absorption ($\tau_{9.7} \sim 1.3$ for VV 340 N). The PAH emission features are prominent in both galaxies, although the 17 μm feature appears much stronger, with respect to the continuum and the fine structure lines, in VV 340 S. Both [Ne V] 14.3 and 24.3 μm lines are seen in the high-resolution spectrum of VV 340 N, as is the [O IV] 25.9 μm line. The line fluxes are 1.2×10^{-17} W m^{-2}, 2.3×10^{-17} W m^{-2}, and 12.3×10^{-17} W m^{-2}, repectively, for the [Ne V] 14.3, 24.3 μm, and [O IV] 25.9 μm lines in VV 340 N. A portion of the Short-High spectra of VV 340 N and S surrounding the location of the [Ne V] 14.3 μm emission line is shown in Figure 4. The [Ne II] 12.8 μm line has a flux of 23.4×10^{-17} W m^{-2} in VV 340 N, and 6.1×10^{-17} W m^{-2} in VV 340 S. In VV 340 N, where the 6.2 μm PAH EQW is 0.48 μm, the [Ne V]/[Ne II] and [O IV]/[Ne II] line flux ratios are consistent with the presence of a weak AGN, contributing less than 10–15% of the IR emission, based on scaling from IRS spectra of local AGN and starburst nuclei (see Armus et al. 2007 and references therein). As the diagnostic ratios are calculated from the nuclear spectrum, this is an upper limit to the contribution from an AGN to the global IR emission in this source. Alternatively, the coronal-line region could be sitting behind at least 50 mag of visual extinction, assuming an intrinsic [Ne V]/[Ne II] flux ratio of unity. This is much larger than that implied by the optical depth at 9.7 μm ($A_V \sim 22$ mag) for VV 340 N. There is no [Ne V] detected from VV 340 S ([Ne V]/[Ne II] < 0.04), and the 6.2 μm PAH EQW is 0.53 μm,

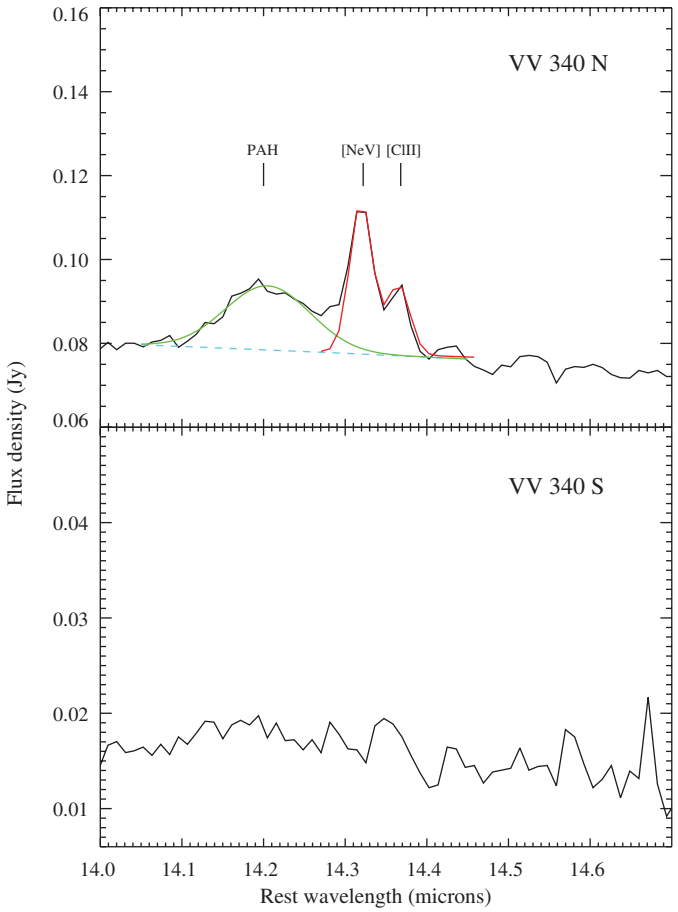

FIG. 4.—IRS Short-High spectra of the nucleus of VV 340 north (*above*), and south (*below*) from 14–14.7 μm in the rest frame. Fits to the PAH 14.22 μm emission feature, as well as the [Ne V] 14.322 μm, and [Cl II] 14.368 μm emission lines indicated in *green* and *red*, respectively in VV 340 N, as is the underlying local continuum (*blue dashed line*). The lines are not detected in VV 340 *S*.

comparable to pure starburst galaxies (Brandl et al. 2006). The lack of [Ne V] emission and the strong PAH EQW both suggest that the southern nucleus has no detectable AGN in the mid-infrared.

The H_2 S(2), S(1), and S(0) rotational lines at 12.28, 17.03, and 28.22 μm are detected in VV 340 N with line fluxes of 5.67×10^{-17} W m^{-2}, 4.56×10^{-17} W m^{-2}, and 1.3×10^{-18} W m^{-2}, respectively. In VV 340 S, only the S(2) and S(1) lines are seen, with fluxes of 4.4×10^{-18} W m^{-2}, and 1.0×10^{-17} W m^{-2}, respectively. Fits to the emission lines imply masses and temperatures for the warm gas components of 1.73×10^7 $M_\odot$ at 530 K in VV 340 N, and 7.8×10^6 $M_\odot$ at 310 K in VV 340 S. The nuclear warm gas fractions (warm/cold) are then $\sim 3 \times 10^{-4}$ and $\sim 7 \times 10^{-4}$ in VV 340 N and VV 340 S, respectively, using the masses of cold H_2 derived by Lo et al. (1997). However, the large extent of the CO emission, 23 kpc in VV 340 N and 10 kpc in VV 340 S (much larger than the IRS slit widths) suggests that these ratios are probably lower limits for the nuclei. The large extent of the CO, the relatively low infrared luminosity to H_2 mass ratio in both galaxies, and the regular kinematics led Lo et al. (1997) to suggest that the VV 340 system is in an early interaction, prestarburst, phase.

VV 340 has a total (north plus south) UV flux of 17.55 mag and 16.64 mag in the far and near-UV GALEX filters, respectively. The pair has an apparent infrared to UV flux ratio (the infrared excess, or IRX), of 81.3. The measured UV slope, β, is -0.38 in the GALEX system (see Kong et al. 2004), placing VV340 well above the fit to local starburst galaxies (Meurer et al. 1999; Goldader et al. 2002) by nearly an order of magnitude. As is obvious from Figure 1, most of the UV emission comes from VV 340 south, while most of the IR emission comes from VV 340 north. If we were to place the galaxies on an IRX-β plot individually, the northern galaxy would have an IRX $\sim$398 and a $\beta \sim -0.39$, while the southern galaxy would have an IRX $\sim$17 and a $\beta \sim -0.44$. This would place the southern source close to the starburst correlation, but the northern source much farther off the correlation than the system as a whole. A full discussion of where the LIRGs fall on the the IRX-β plot is given in Howell et al. (2009).

VV 340 is detected at both 1.49 and 4.85 GHz with the VLA (Condon et al. 1990; 1995). While both VV 340 N and S are resolved in the VLA C-array data, the A-array data also reveal a nuclear component and two "hotspots" at radii of about 5″, oriented N-S along the edge-on disk of VV 340 N. VV 340 N and VV 340 S have 1.49 GHz flux densities of 86, and 12 mJy, respectively, and 4.85 GHz flux densities of 30 and 3.5 mJy, respectively. The system has a logarithmic far-infrared to radio flux ratio, q (Helou et al. 1985) of $q = 2.02$ dex. This is within 1.5 σ of the standard value for star-forming galaxies ($q = 2.34 \pm 0.26$ dex; Yun et al. 2001). VV 340 N and VV 340 S have q values of 2.02 and 2.00 dex, respectively. VV 340 S has a slightly steeper radio spectral index ($\alpha = -1.0$) than does VV 340 N ($\alpha = -0.8$), the latter being comparable to the standard value seen in star-forming galaxies (Condon 1992).

Chandra X-ray imaging of VV 340 is shown in Figures 5 and 6. While both galaxies are detected, the emission from the southern galaxy is much weaker, and more diffuse. The northern galaxy is clearly resolved in the soft bands (0.5–2 keV), with a size of nearly 25″ (17 kpc), but shows a hard (2–7 keV) X-ray point source coincident with the nucleus. The hard X-ray image also shows two faint blobs to the north and south, aligned with the radio structure (Condon et al. 1990).

The X-ray spectrum of VV 340 N (Fig. 7) is dominated by emission-line rich, extended soft X-ray emission but an excess at high energies above 4 keV is evident. In Figure 7 we compare the *Chandra* spectrum of VV 340 N to that of the starburst-dominated LIRG VII Zw 31 (Iwasawa et al. 2009b, in preparation). VII Zw 31 shows no hard-band excess above 4 keV. The

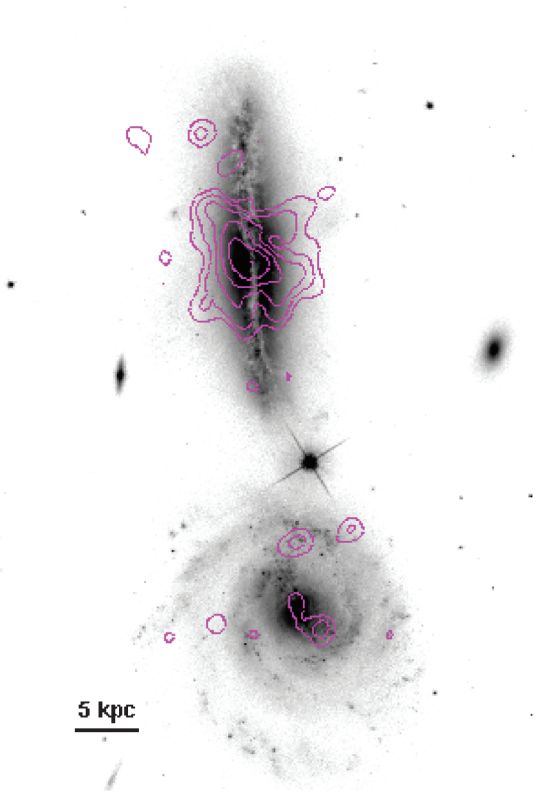

FIG. 5.—Soft (0.2–5 keV) X-ray image of VV 340 taken with the *Chandra X-Ray Observatory* (*contours*), overlaid on the HST ACS F435W image (*greyscale*). North is up, and east is to the left.

hard-band excess in VV 340 N peaks at approximately 6.4 keV in the rest frame, suggesting a pronounced Fe K line. With the limited detected counts, the exact spectral shape cannot be constrained. However, the most likely interpretation for this hard excess is the emission from a heavily absorbed active nucleus with an absorbing column density ($N_{\rm H}$) of 10^{24} cm^{-2} or larger. Note, this is significantly larger than that implied by the silicate optical depth at 9.7 μm. If the observed emission is reflected light from a Compton thick AGN, the intrinsic luminosity could be as high as 2×10^{41} erg s^{-1} in the 2–7 keV band. There is

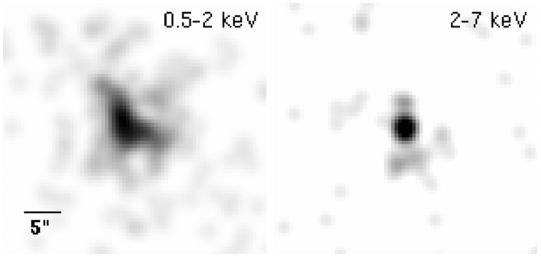

FIG. 6.—The soft (*left*) and hard (*right*) X-ray images of VV 340 north taken with the *Chandra X-Ray Observatory*. The images have been smoothed with a Gaussian kernel with $\sigma = 2$ pixels. The orientation of the image is north up and east to the left.

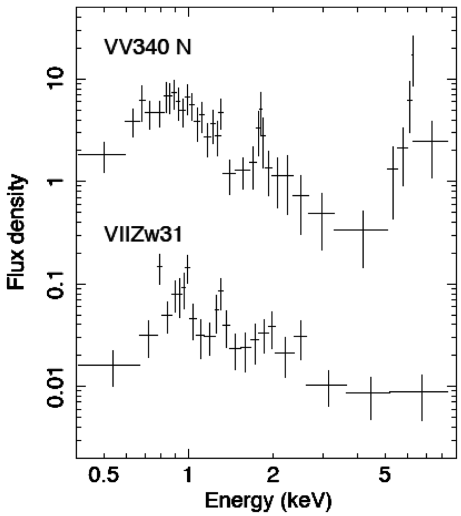

FIG. 7.—The X-ray spectrum of VV 340 north obtained from the ACIS-S. For display purposes, the original data have been rebinned so that each spectral bin contains at least five counts. The vertical axis is in units of 10^{-14} erg cm^{-2} s^{-1} keV^{-1}. Also included for comparison is the ACIS-S spectrum of VII Zw 31 from Iwasawa et al. (2009b, in preparation), scaled by 0.02, which is an example of a starburst-dominated LIRG. The hard X-ray excess in VV 340 north is evident at energies above about 4 keV.

also evidence for the 1.8 keV Si line, which could have a contribution from AGN photoionization, although it could also signal the presence of a large number of core-collapse SNe.

Taken together, the *Spitzer, Chandra, GALEX, HST,* and VLA data suggest that the interacting system VV 340 is composed of two very different galaxies. The edge-on disk of VV 340 north hides a buried AGN seen in the mid-infrared and X-rays, although the apparent contribution of this AGN to the total energy of the galaxy is low. In contrast, VV 340 south is a face-on starburst galaxy that generates an order of magnitude less far-infrared flux, but dominates the short-wavelength UV emission from the system. VV 340 is a LIRG because of the enhanced emission coming from VV 340 N alone. VV 340 seems to be an excellent example of a pair of interacting galaxies evolving along different paths, or at different rates, implying that the details of the interaction can produce LIRGs whose global properties mask the true nature of the emission. This is particularly relevant for merging galaxies viewed at high redshift.

The *Spitzer Space Telescope* is operated by the Jet Propulsion Laboratory, California Institute of Technology, under NASA contract 1407. This research has made use of the NASA/IPAC Extragalactic Database (NED) which is operated by the Jet Propulsion Laboratory, California Institute of Technology, under contract with the National Aeronautics and Space Administration. Based on observations made with the NASA Galaxy Evolution Explorer. *GALEX* is operated for NASA by the California Institute of Technology under NASA contract NAS5-98034. TV, ASE, and DCK were supported by NSF

grant AST 02-06262 and by NASA through grants HST-GO10592.01-A and HST-GO11196.01-A from the Space Telescope Science Institute, which is operated by the Association of Universities for Research in Astronomy under NASA contract NAS5-26555. TV and HI acknowledge support from the IPAC Graduate Student Fellowship Program. The authors wish to thank an anonymous referee for suggestions which improved the manuscript.

REFERENCES

Armus, L., Charmandaris, V., Bernard-Salas, J., et al. 2007, ApJ, 656, 148
Armus, L., Charmandaris, V., Spoon, H., et al. 2004, ApJS, 154, 178
Armus, L., Heckman, T. M., & Miley, G. K. 1987, AJ, 94, 831
———. 1989, ApJ, 347, 727
Armus, L., et al. 2006, ApJ, 640, 204
Barnes, J. E., & Hernquist, L. 1992, ARA&A, 30, 705
Blain, A. W., Smail, I., Ivison, R. J., Kneib, J.-P., & Frayer, D. T. 2002, Phys. Rep., 369, 111
Brandl, B., et al. 2006, ApJ, 653, 1129
Bushouse, H. A., & Stanford, S. A. 1992, ApJS, 79, 213
Caputi, K. I., Lagache, G., Yan, L., et al. 2007, ApJ, 660, 97
Chapman, S. C., Blain, A. W., Smail, I., & Ivison, R. J. 2005, ApJ, 622, 772
Condon, J. J. 1992, Annu. Rev. Astron. Astrophys., 30, 575
Condon, J. J., Anderson, E., & Broderick, J. J. 1995, AJ, 109, 2318
Condon, J. J., Helou, G., Sanders, D. B., & Soifer 1990, ApJS, 73, 359
Dahlem, M., Weaver, K. A., & Heckman, T. M. 1998, ApJS, 118, 401
Desai, V., Armus, L., Spoon, H., et al. 2007, ApJ, 669, 810
Dickinson, M., et al. 2003, in The Mass of Galaxies at Low and High Redshift ESO Astrophysics Symp., ed. R. Bender, & A. Renzini, Springer-Verlag, 324
Draine, B. T., & Li, A. 2001, ApJ, 551, 807
Dunne, L., Eales, S., Edmunds, M., et al. 2000, MNRAS, 315, 115
Elbaz, D., Cesarsky, C., Chanial, P., et al. 2002, A&A, 384, 848
Evans, A. S., Mazzarella, J. M., Surace, J. A., Frayer, D. T., Iwasawa, K., & Sanders, D. B. 2005, ApJS, 158, 197
Evans, A. S., Vavilkin, T., Pizagno, J., et al. 2008, ApJ, 675, L69
Fabbiano, G., Heckman, T. M., & Keel, W. C. 1990, ApJ, 355, 442
Ferrarese, L., & Merritt, D. 2000, ApJ, 539, L9
Gao, Y., & Solomon, P. M. 2004, ApJ, 606, 271
Gebhardt, K., Bender, R., Bower, G., et al. 2000, ApJ, 539, L13
Genzel, R., Lutz, D., Sturm, E., Egami, E., & Kunze, D., et al. 1998, ApJ, 498, 589
Genzel, R., Tacconi, L. J., Rigopoulou, D., Lutz, D., & Tecza, M. 2001, ApJ, 563, 527
Gil de Paz, A., Boissier, S., Madore, B., et al. 2007, ApJS, 173, 185
Goldader, J. D., Meurer, G., Heckman, T., et al. 2002, ApJ, 568, 651
Grimm, H.-J., Gilfanov, M., & Sunyaev, R. 2003, MNRAS, 339, 793
Heckman, T. M., Armus, L., & Miley, G. K. 1990, ApJ Suppl., 74, 833
Helou, G., Soifer, B. T., & Rowan-Robinson, M. 1985, ApJ, 298, L7
Hinshaw, G., Weiland, J., Hill, R., et al. 2009, ApJS, 180, 225
Houck, J. R., Roellig, T., van Cleve, J., et al. 2004, ApJS, 154, 18
Howell, J. H., et al. 2009, ApJ, submitted
Ishida, C. 2004, Ph.D. thesis, Univ. Hawaii
Iwasawa, K., Sanders, D. B., Evans, A. S., Mazzarella, J. M., Armus, L., & Surace, J. 2009a, ApJ, 695, L103
Kim, D.-C., Sanders, D. B., Veilleux, S., Mazzarella, J. M., & Soifer, B. T. 1995, ApJS, 98, 129
Kim, D.-C., Veilleux, S., & Sanders, D. B. 1998, ApJ, 508, 627
Komossa, S., Burwitz, V., Hasinger, G., et al. 2003, ApJ, 582, L15
Kong, X., Charlot, S., Brinchmann, J., et al. 2004, MNRAS, 349, 769
Lacy, M., Storrie-Lombardi, L.., Sajina, A., et al. 2004, ApJS, 154, 166
Lahuis, F., Spoon, H., Tielens, A., et al. 2007, ApJ, 659, 296
Le Floch, E., Papovich, C., Dole, H., et al. 2005, ApJ, 632, 169
Levenson, N. A., Sirocky, M., Hao, L., et al. 2007, ApJ, 654, L45
Lo, K. Y., Gao, Y., & Gruendl, R. A. 1997, ApJ, 475, L103
Magnelli, B., Elbaz, D., et al. 2009, A&A, 496, 57
Martin, D. C., Small, T., Schiminovich, D., et al. 2007, ApJS, 173, 415
Mazzarella, J. M., & Balzano, V. A. 1986, ApJS, 62, 751
Mazzarella, J. M., Graham, J. R., Sanders, D. B., & Djorgovski, S. 1993, ApJ, 409, 170
Mengel, S., Lehnert, M. D., Thatte, N., & R., Genzel 2005, A&A, 443, 41
Mengel, S., Lehnert, M. D., Thatte, N., Tacconi-Garman, L., & Genzel, R. 2001, ApJ, 550, 280
Meurer, G. R., Heckman, T. M., & Calzetti, D. 1999, ApJ, 521, 64
Mirabel, I. F., Vigroux, L., Charmandaris, V., et al. 1998, A&A, 333, L1
Mould, J. R., Huchra, J., Freedman, W., et al. 2000, ApJ, 529, 786
Murphy, E. J., Helou, G., Braun, R., et al. 2006, ApJ, 651, L111
Murphy, T. W., Jr., Armus, L., Matthews, K., Soifer, B. T., Mazzarella, J. M., Shupe, D. L., Strauss, M. A., & Neugebauer, G. 1996, AJ, 111, 1025
Murphy, T. W., Jr., Soifer, B. T., Matthews, K., & Armus, L. 2001a, ApJ, 559, 201
Murphy, T. W., Jr., Soifer, B. T., Matthews, K., Armus, L., & Kiger, J. R. 2001b, AJ, 121, 97
Murphy, T. W., Jr., Soifer, B. T., Matthews, K., Kiger, J. R., & Armus, L. 1999, ApJ, 525, L85
Ranalli, P., Comastri, A., & Setti, G. 2003, A&A, 399, 39
Read, A. M., Ponman, T. J., & Strickland, D. K. 1997, MNRAS, 286, 626
Rhoads, J. E. 2000, PASP, 112, 703
Sanders, D. B., Mazzarella, J. M., Kim, D.-C., Surace, J. A., & Soifer, B. T. 2003, AJ, 126, 1607
Sanders, D. B., & Mirabel, I. F. 1996, ARA&A, 34, 749
Sanders, D. B., Scoville, N. Z., & Soifer, B. T. 1991, ApJ, 370, 158
Sanders, D. B., Soifer, B. T., Elias, J. H., Madore, B. F., et al. 1988a, ApJ, 325, 74
Sanders, D. B., Soifer, B. T., Elias, J. H., Neugebauer, G., & Matthews, K. 1988b, ApJ, 328, L35
Schecter, P. 1976, ApJ, 203, 297
Schiminovich, D., Wyder, T., Martin, D., et al. 2007, ApJS, 173, 315
Schmidt, M., & Green, R. F. 1983, ApJ, 269, 352
Scoville, N., Aussel, H., Brusa, M., et al. 2007, ApJS, 172, 1
Sirocky, M. M., Levenson, N. A., Elitzur, M., Spoon, H. W. W., & Armus, L. 2008, ApJ, 678, 729
Skrutskie, M. F., Cutri, R., Stiening, R., et al. 2006, AJ, 131, 1163
Smith, J. D., Draine, B., Dale, D., et al. 2007, ApJ, 656, 770

Spoon, H. W. W. W., Armus, L., Cami, J., et al. 2004, ApJS, 154, 184
Spoon, H. W. W. W., Tielens, A., Armus, L., et al. 2006, ApJ, 638, 759
Stern, D., Eisenhardt, P., Gorjian, V., et al. 2005 ApJ, 631, 163
Strickland, D. K., Heckman, T. M., Colbert, E. J. M., Hoopes, C. G., & Weaver, K. A. 2004a, ApJS, 151, 193
———. 2004b, ApJ, 606, 829
Sturm, E., Lutz, D., Verma, A., et al. 2002, A&A, 393, 821
Tacconi, L. J., Genzel, R., Lutz, D., et al. 2002, ApJ, 580, 73
Teng, S. H., et al. 2009, ApJ, in press
Tran, Q. D., Lutz, D., Genzel, R., et al. 2001, ApJ, 552, 527
van Dokkum, P. 2001, PASP, 114, 1420
Veilleux, S., Kim, D. C., Sanders, D. B., Mazzarella, J. M., & Soifer, B. T. 1995, ApJS, 98, 171
Veilleux, S., Sanders, D. B., & Kim, D.-C. 1997, ApJ, 484, 92
Whitmore, B. C., Gilmore, D., Leitherer, C., et al. 2005, AJ, 130, 2104
Whitmore, B. C., Rupali, C., & Fall, M. S. 2007, AJ, 133, 1067
Whitmore, B. C., & Schweizer, F. 1995, AJ, 109, 960
Wright, G. S., James, P. A., Joseph, R. D., & McLean, I. S. 1990, Nature, 344, 417
Xu, C. K., Shupe, D., Buat, V., et al. 2007, ApJS, 173, 432
Yun, M. S., Reddy, N. A., Condon, J. J., & 2001, ApJ, 554, 803